



A PHOTOGRAMMETRY-BASED HYBRID SYSTEM FOR DYNAMIC TRACKING AND  
MEASUREMENT

THESIS

Daniel P. Magree, Civilian

AFIT/GAE/ENY/10-J01

DEPARTMENT OF THE AIR FORCE  
AIR UNIVERSITY

**AIR FORCE INSTITUTE OF TECHNOLOGY**

Wright-Patterson Air Force Base, Ohio

APPROVED FOR PUBLIC RELEASE; DISTRIBUTION UNLIMITED.

The views expressed in this thesis are those of the author and do not reflect the official policy or position of the United States Air Force, Department of Defense, or the United States Government. This material is declared a work of the U.S. Government and is not subject to copyright protection in the United States

AFIT/GAE/ENY/10-J01

A PHOTOGRAMMETRY-BASED HYBRID SYSTEM FOR DYNAMIC TRACKING AND  
MEASUREMENT

THESIS

Presented to the Faculty

Department of Aeronautical and Astronautical Engineering

Graduate School of Engineering and Management

Air Force Institute of Technology

Air University

Air Education and Training Command

In Partial Fulfillment of the Requirements for the  
Degree of Master of Science in Aeronautical Engineering

Daniel P. Magree, BS

Civilian

June 2010

APPROVED FOR PUBLIC RELEASE; DISTRIBUTION UNLIMITED.

AFIT/GAE/ENY/10-J01

A PHOTOGRAMMETRY-BASED HYBRID SYSTEM FOR DYNAMIC TRACKING AND  
MEASUREMENT

Daniel P. Magree, BS  
Civilian

Approved:

//signed//

---

Jonathan T. Black, PhD (Chairman)

14 June 2010

---

Date

//signed//

---

Lt Col Eric D. Swenson (Member)

14 June 2010

---

Date

//signed//

---

Mark F. Reeder, PhD (Member)

14 June 2010

---

Date



*Abstract*

Noncontact measurements of lightweight flexible aerospace structures present several challenges. Objects are usually mounted on a test stand because current noncontact measurement techniques require that the net motion of the object be zero. However, it is often desirable to take measurements of the object under operational conditions, and in the case of miniature aerial vehicles (MAVs) and deploying space structures, the test article will undergo significant translational motion. This thesis describes a hybrid noncontact measurement system which will enable measurement of structural kinematics of an object freely moving about a volume. By using a real-time videogrammetry system, a set of pan-tilt-zoom (PTZ) cameras is coordinated to track large-scale net motion and produce high-speed, high-quality images for photogrammetric surface reconstruction. The design of the system is presented in detail. A method of generating the calibration parameters for the PTZ cameras is presented and evaluated and is shown to produce good results. The results of camera synchronization tests and tracking accuracy evaluation are presented as well. Finally, a demonstration of the hybrid system is presented in which all four PTZ cameras track an MAV in flight.

## *Acknowledgements*

There are many people I am indebted to for their help and advice in the production of this thesis. I would first of all like to thank my advisor, Dr. Jonathan Black, for his guidance throughout my time at AFIT and especially during the final months. My committee members Dr. Reeder and Lt Col Swenson provided helpful criticism and advice during the preparation of the final document. My research colleagues Alan Jennings, Chris Allen, and Greg Briggs contributed their time and effort to this project and this document would not have been possible without their support. I would like to thank the Air Force Research Laboratories and the Air Force Office of Scientific Research for sponsoring this research and supporting me financially during my time at AFIT. Finally, I would like to thank God, who made reality understandable and gave us the desire to understand it.

Daniel P. Magree

# *Table of Contents*

	Page
Abstract . . . . .	iv
Acknowledgements . . . . .	v
List of Figures . . . . .	viii
List of Tables . . . . .	xi
I. Introduction . . . . .	1
II. Background . . . . .	4
2.1 Photogrammetry . . . . .	4
2.1.1 Pinhole camera model . . . . .	5
2.1.2 Extended camera model . . . . .	8
2.1.3 Camera calibration . . . . .	11
2.1.4 Videogrammetry . . . . .	12
2.1.5 Applications of photogrammetry to membrane struc- tures measurement . . . . .	13
2.2 Comparison with Other Noncontact Measurement Systems . . . . .	15
2.3 Hybrid Measurement Systems . . . . .	17
III. System Design and Development . . . . .	19
3.1 System Overview . . . . .	19
3.2 Videogrammetry System . . . . .	20
3.3 Camera Gimbals . . . . .	22
3.3.1 Camera aiming . . . . .	22
3.3.2 Camera location . . . . .	23
3.4 Lens . . . . .	33
3.5 Camera . . . . .	36
3.6 Computers and Software . . . . .	37
3.7 Image Processing . . . . .	40
3.8 Test Equipment . . . . .	40
IV. System Tests and Results . . . . .	41
4.1 Camera Calibration . . . . .	41
4.2 Development of Parameter Curves . . . . .	41
4.3 Test of Curve-fit Parameters . . . . .	44
4.4 Validation of Image Synchronization . . . . .	51
4.5 Validation of Tracking System . . . . .	51
4.6 Tracking Example: Helicopter . . . . .	59

	Page
V. Conclusions and Future Work . . . . .	66
5.1 Conclusion . . . . .	66
5.2 Future Work . . . . .	67
Bibliography . . . . .	69

## *List of Figures*

Figure		Page
2.1	Schematic of a pinhole camera. . . . .	7
2.2	Effect of pincushion (a) and barrel (b) radial distortion on image points. Crosses represent undistorted points and circles show the effect of distortion . . . . .	10
2.3	Effect of decentering distortion on image points. Crosses represent undistorted points and circles show the effect of distortion . . . . .	10
3.1	The DTM system consists of a videogrammetry subsystem for real-time motion capture and four pan-tilt-zoom camera subsystems. . . . .	19
3.2	Videogrammetry cameras are setup around the room's perimeter and track body motion. Each tracking subsystem uses this data to focus at the moving point. . . . .	20
3.3	A camera subsystem consists of a two axis gimbal, zoom-focus lens, a high speed camera, and controller computer (not shown). . . . .	20
3.4	Samples can be mounted on a platform that maintains orientation while moving through a circular path. . . . .	21
3.5	Calibration wand used to calibrate and set the origin of the videogrammetry system . . . . .	22
3.6	Vector $\vec{r}$ is the distance between the gimbal and test object, and is transformed into gimbal body coordinate system to calculate azimuth and elevation angles. . . . .	23
3.7	Videogrammetry object is aligned with $x$ axis and $y$ camera coordinate is adjusted, then the object is moved off-axis and the $x$ coordinated is adjusted. . . . .	24
3.8	Targeted object used for camera location. Retroreflective and coded targets are shown. The VOCS and PCS $x$ and $y$ axes are shown, with the origin at their intersection and the $z$ axis oriented so as to form a right hand coordinate system. . . . .	26
3.9	Planar graphs of camera locations with respect to hand location point (denoted by circle). Blue x denotes project one and two points. Red square denotes project three points, found after rotating camera. Scale is in millimeters. . . . .	31
3.10	Relation of the gimbal rotation axes (red) to the optical axis and approximate focal point of the camera (blue). The gimbal $x$ axis and the optical axis are parallel (but not collinear) when the gimbal is at zero azimuth and elevation. . . . .	32
3.11	Graph of data and curve fits for magnification and focus polynomial coefficients . . . . .	35

3.12	Graph showing the magnification and focus data (blue), the curve fit approximations (red) and the typical domain of the lens settings in the current lab (green). . . . .	35
3.13	Schematic describing the calculation of magnification and focus settings .	36
3.14	System software and hardware communication . . . . .	38
3.15	The lens, gimbal and lens and gimbal state recording is controlled with the interface shown. . . . .	38
4.1	Graphs showing calibration parameter data and curve fits. Error bars are based on calibration quality and determine weights given to data points	43
4.2	PhotoModeler calibration grid. 8-12 images of the grid from different angles are processed to generate calibration parameters at a specific lens setting. . . . .	45
4.3	Approximate camera locations for lens condition one and two. Lens condition three did not have the four locations with highest angle of incidence. . . . .	46
4.4	Residual direction and relative scale of each point in each image for PC point cloud in test one . . . . .	48
4.5	Residual direction and relative scale of each point in each image for CF point cloud in test one . . . . .	48
4.6	Error for four photogrammetry projects compared to the truth surface. Circles denote raw points and triangles denote points scaled, translated and rotated for optimum fit. Points are plotted against scalar distance from origin. The object is rotated 90° between each position. . . . .	52
4.7	The four high-speed cameras capturing synchronous images at 500fps. Note that the spinning paper “fan” has the same orientation with respect to the mounting platform in each image. . . . .	53
4.8	Camera aiming error is measured in pixels from the center image pixel to the coded target on the box. . . . .	56
4.9	RMS mm error vs speed of rotation table. Points marked with x’s were tested at 2.5 m from camera. Diamond points indicate tests run at increased distances. . . . .	56
4.10	RMS Angular error vs. RMS angular velocity of gimbal. Points marked with x’s were tested at 2.5 m from camera. Diamond points indicate tests run at increased distances. . . . .	57
4.11	Bode plots of tracking data. Points marked with x’s were tested at 2.5 m from camera. Diamond points indicate tests run at increased distances.	61
4.12	Resolution as a function of object speed and size, assuming ideal lens operation. . . . .	62
4.13	Twin rotor helicopter used in example capture . . . . .	62
4.14	Helicopter and camera $x$ - $y$ locations during image capture . . . . .	63

	Page
4.15 Helicopter speed and height during image capture . . . . .	63
4.16 Images of helicopter from camera 4 at one second intervals . . . . .	64
4.17 Images of helicopter from camera 4 at one second intervals . . . . .	65

## *List of Tables*

Table		Page
3.1	Data from camera location by photogrammetry . . . . .	30
4.1	Data on the calibration grid used in the curve-fit tests . . . . .	44
4.2	Comparison of point cloud data at lens condition 1 . . . . .	49
4.3	Comparison of point cloud data at lens condition 2 . . . . .	49
4.4	Comparison of point cloud data at lens condition 3 . . . . .	50



# A PHOTOGRAMMETRY-BASED HYBRID SYSTEM FOR DYNAMIC TRACKING AND MEASUREMENT

## I. Introduction

LIGHTWEIGHT membranes and structures are drawing increased interest for use in a variety of applications. Membranes and inflatable structures are part of many proposed satellite concepts serving a variety of purposes such as antenna, solar sails, and heat shields. These materials are intended to be compactly stored for launch and then unfurl once in space. When fully deployed, the structures will need to be able to resist disturbance caused by accelerations of the spacecraft, electromagnetic momentum, and other events. Miniature aerial vehicles (MAVs) are a new class of flight vehicles with dimensions typically less than 1 m. Because of their low Reynolds number flight regime, MAVs require a novel design approach. Lightweight, flexible material is now not only tolerated but also designed into the aircraft and plays a key role in the achieving the desired flight characteristics of the vehicle. The prevalence of flexible and flapping wings on flying animals illustrate their usefulness and possible optimality for flight at this scale.

For effective design and operation of satellites and MAVs, measurements must be taken of their response under normal operating conditions and anomalous disturbances. A satellite operator must be able to tell whether his deployable structure has deployed correctly. Resonant frequencies of the structures must be known and designed around. Effects such as wrinkling must be detected, as they can affect structure performance. MAV designers are still wrestling with the generation of accurate computer models for flight at Reynolds number on the order of  $10^4$  and lower, and require flight data to validate these models. However, lightweight structures pose significant measurement challenges. Large membranes have large displacement, long-period dynamics that are difficult to measure with traditional equipment such as strain gages. Small structures are of comparable weight to the gages themselves, and attaching them to the structure

affects the dynamic response. Adding sensors to MAVs for in-flight testing is impractical because of payload weight limits.

Noncontact measurement methods are a logical solution to the measurement difficulties described above. There are many noncontact measurement methods in use today. Laser vibrometry, the measurement of velocity of an object based the interference of the a laser beam with the reflected response from an object, is the standard for dynamic measurements, boasting high spacial resolution and sampling frequency. Photogrammetry is the process of deriving the three-dimensional coordinates of object points based on their two dimensional location in a set of photographic images, and is increasingly in use as computer processing and digital imaging technology matures. Other methods such as laser range finders, capacitance measurement, and various interferometry techniques are also found in the literature. These techniques are discussed in greater detail in the next chapter. All of these techniques have their strengths and weaknesses, and none of them represent a complete solution to the problem of membrane measurement. Laser vibrometry has difficulty with large displacement of large membrane structures and the high sampling frequency would be unnecessary. Capacitance and interferometry techniques require very flat, and in the case of capacitance, conductive, material. The accuracy of photogrammetry methods are limited by camera resolution, and processing can often be labor intensive. The optical characteristics of the material itself, such as reflectance or transparency, can make measurement difficult. All of the above measurement techniques would be difficult to use on a dynamic object such as a MAV in flight or an extending satellite boom.

Therefore, new measurement techniques must be developed confront these limitations. Many of the limitations can be solved with creative application of current techniques. For instance, recent research has enabled the use of photogrammetry on transparent membranes [1]. Also, combining data from different sensors has been investigated to overcome the limitations of the individual measurement systems [2].

This thesis proposes a solution to one lightweight structures measurement problem in particular: Surface reconstruction of an object that is dynamically moving throughout a volume. Examples include measurement of the wing shape of a flapping MAV in free

flight, wing flex on a fixed-wing MAV, deployment of a solar sail, and deployment of a boom. A hybrid measurement system approach is taken, in which large-scale motion of the object is measured by a real-time videogrammetry system and used to direct four pan-tilt-zoom (PTZ) cameras for taking high-resolution images of the area of interest. The image data is then processed with photogrammetry software with which a dense surface profile is generated. The work of this thesis was to build this system, test and evaluate its capabilities, and establish that this approach will produce effective image data and system state information for the accurate reconstruction of lightweight dynamic structures.

This document is arranged as follows: Chapter 2 presents the review of current lightweight structures measurement research, with a particular focus on photogrammetry. Chapter 3 describes in detail the components of the measurement system, their operation and integration. Chapter 4 presents the tests performed to validate the system and determine its capabilities, and the results of the tests. Chapter 5 presents the conclusions drawn from the research and suggests directions for future work.

## II. Background

WITH the increased use of and interest in lightweight structures, there has been a significant amount of research undertaken into the development of noncontact shape measurement systems. These measurement systems vary greatly in accuracy, ease of use, and adaptability, and so the choice of measurement system is highly application-dependent. Many noncontact measurement systems have been investigated for their suitability for the measurement of miniature aerial vehicle wing surface profiles and lightweight space structures. This chapter presents an overview of the current state of the art in noncontact measurement systems as they relate to these applications.

Methods that have gained considerable attention recently are photogrammetry and its relative, videogrammetry. These methods form the basis of the hybrid measurement system that is the work of this thesis, and will be discussed in detail. Additional methods such as laser vibrometry and range finding, Moire fringe projection and capacitance are also found in the literature and these are compared to photogrammetry techniques. Finally, research into hybrid systems including two or more measurement techniques is presented.

### ***2.1 Photogrammetry***

Photogrammetry is the process of deriving the three-dimensional coordinates of object points based on their two dimensional location in a set of photographic images. Photogrammetry has its origins in the mid-1800s, following immediately the invention of direct photography by Louis Daguerre [3]. Photogrammetry developed gradually through the early part of the 20th century, due to the difficulty of working with photographic film, but still many high precision analog systems were developed for use in surveying and map making, along with the mathematical principles of photogrammetric triangulation and error evaluation. The last 30 years have seen the advent of inexpensive digital computing and photography, as well as advances in optics, which has allowed greater versatility and automation of the photogrammetric process [4]. Photogrammetry is now used for applications as varied as robot vision, as-built facilities measurement, digitization of cultural artifacts, and biometrics analysis [5].

Photogrammetry techniques can be divided into two main categories: target-based and texture-based. Target-based photogrammetry requires the use of physical or projected marks on an object to aid in point referencing between images. The targets are designed to appear as high contrast points in the images, and so are easy for imaging software to identify. To further automate processing, some systems use coded targets which can be directly referenced between images. Texture-based photogrammetry uses natural or projected texture of the object to correlate points between a set of images. This process produces a denser set of point data than target-based methods, but is less automated and more object-dependent. In order to be suitable for texture-based methods, the surface of the object must have sufficient contrast variation to be identifiable to the correlation software. Furthermore, the image angle plays a large role in the identification and correlation of points between images [6].

In either case, the fundamental problem of photogrammetry is to determine the relationship between the photographed objects and the captured image. The captured image is the result of collecting and recording electromagnetic radiation reflected (or emitted) by the objects. Therefore, the relationship between image and objects should describe the path of rays between the object and imaging sensor. The relationship is described by a camera model and an atmospheric model. For close range photogrammetry, the atmosphere is assumed to have a negligible effect on the path of the rays, and thus the relationship is completely described by the camera model [3]. The development of the camera model is presented in the next section.

*2.1.1 Pinhole camera model.* Most camera models are based on an ideal pinhole camera. A schematic of a pinhole camera is shown in Figure 2.1. A pinhole camera has no lens, rather light passes through a point (the pinhole) in the front of the camera and illuminates the imaging plane. By passing all rays through the same point, each position on the screen is illuminated by rays from only one direction. The pinhole is called the focal point or perspective center. For the theoretical model, the imaging plane can be moved in front of the focal point so that the image appears as it would in a photographic print. The line normal to the imaging plane that passes through the focal point is called

the optical axis, and the point at which it intersects the imaging plane is the principle point. The distance along the optical axis between the imaging plane and the focal point is the focal length or principal distance.

The camera imaging process can be described mathematically as the perspective projection of three-dimensional points onto a two-dimensional plane. Consider the imaging plane and the three-dimensional world points to be represented by two coordinate systems whose origins are at the focal point. The imaging plane coordinate system (ICS)  $x$  and  $y$  axes lie in a plane parallel to the image plane with the  $x$  axis pointing towards right side of the image plane and the  $y$  axis pointing towards the top. The  $z$  axis is aligned with the optical axis. The global coordinate system (GCS) can have any orientation. The transformation of a point  $[XYZ]$  in GCS to point  $[xyz]$  in ICS is described by

$$M \begin{bmatrix} X \\ Y \\ Z \end{bmatrix} = \frac{1}{k} \begin{bmatrix} x \\ y \\ z \end{bmatrix} \quad (2.1)$$

where  $M$  is a 3x3 rotation matrix defined by Euler angles  $\phi$ ,  $\theta$ , and  $\psi$  that rotates GCS into ICS, and  $k$  is a scale factor between the coordinate systems. The  $z$  coordinate of all points in the image plane is equal to the negative of the focal length, and since the GCS origin does not typically coincide with the focal point, translational terms  $X_L$ ,  $Y_L$ , and  $Z_L$  are introduced

$$M \begin{bmatrix} X - X_L \\ Y - Y_L \\ Z - Z_L \end{bmatrix} = \frac{1}{k} \begin{bmatrix} x \\ y \\ -f \end{bmatrix} \quad (2.2)$$

The values of  $X_L$ ,  $Y_L$ , and  $Z_L$  and  $\phi$ ,  $\theta$ , and  $\psi$  are known as external camera parameters [4]. If matrix  $M$  is made up of elements  $m_{i,j}$ , Equation 2.2 can be rewritten as three

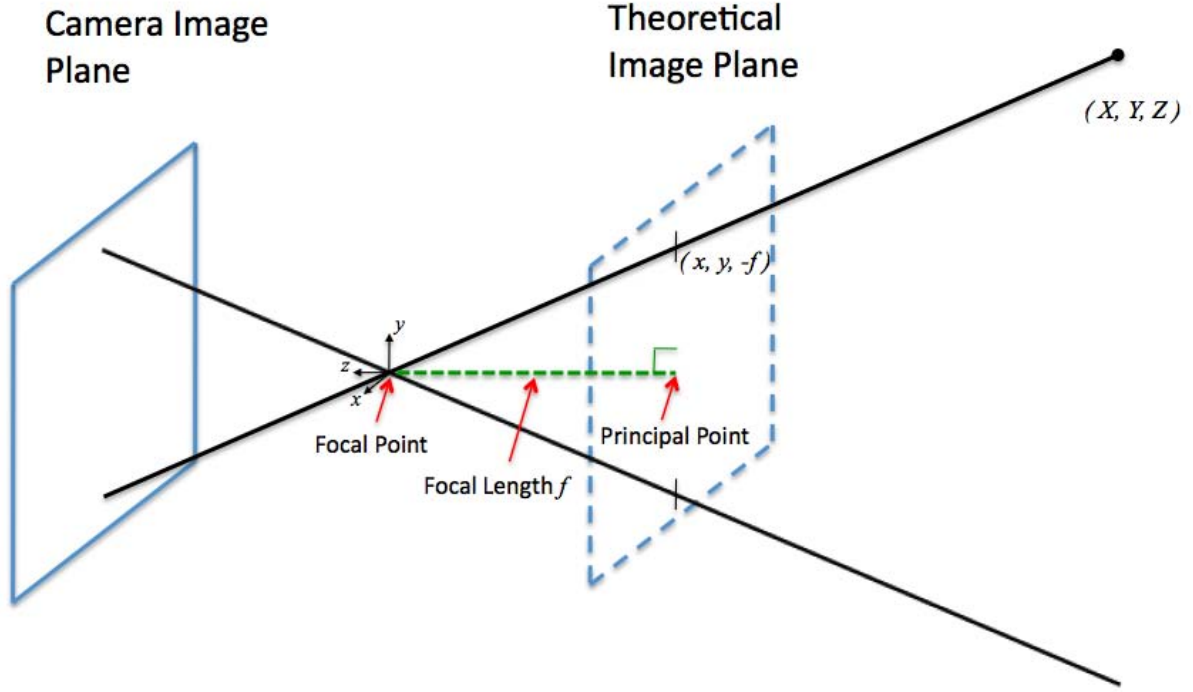


Figure 2.1: Schematic of a pinhole camera.

equations

$$x = k[m_{1,1}(X - X_L) + m_{1,2}(Y - Y_L) + m_{1,3}(Z - Z_L)] \quad (2.3)$$

$$y = k[m_{2,1}(X - X_L) + m_{2,2}(Y - Y_L) + m_{2,3}(Z - Z_L)] \quad (2.4)$$

$$-f = k[m_{3,1}(X - X_L) + m_{3,2}(Y - Y_L) + m_{3,3}(Z - Z_L)] \quad (2.5)$$

and eliminating scale factor  $k$  leaves

$$x = -f \frac{m_{1,1}(X - X_L) + m_{1,2}(Y - Y_L) + m_{1,3}(Z - Z_L)}{m_{3,1}(X - X_L) + m_{3,2}(Y - Y_L) + m_{3,3}(Z - Z_L)} \quad (2.6)$$

$$y = -f \frac{m_{2,1}(X - X_L) + m_{2,2}(Y - Y_L) + m_{2,3}(Z - Z_L)}{m_{3,1}(X - X_L) + m_{3,2}(Y - Y_L) + m_{3,3}(Z - Z_L)} \quad (2.7)$$

Equations 2.6 and 2.7 are called the collinearity equations, referring to the fact that the object point, focal point and image point lie along the same line. These equations form the basis of most photogrammetry techniques, and can be used to solve several types of

problems depending on which variables are considered known and unknowns. Unknowns are solved for using an optimization routine, which is known as bundle adjustment.

3-D point determination can be performed with as few as two cameras, but using additional cameras allows for self-validation of the point location results. The bundle adjustment produces point locations that are the optimal solution to the collinearity equation system based on the image points, and statistical evaluation of the solution can determine precision confidence. The optimal solution points do not coincide exactly with the location calculated from each photo, and the residual error between image points and solution points is used to calculate confidence in the point locations. Precision estimation is a useful feature of photogrammetry techniques.

*2.1.2 Extended camera model.* The ideal camera model assumes a perfect projection from the object point to the image plane; however, in reality this is not the case. Causes of error in the projection include lens distortion, misalignment of the lens, lens imperfections, and non-flat image sensor. If the effects of these flaws can be modeled then the ideal camera model can be modified to produce more accurate results. Commonly modeled error effects in the literature are principle point shift, radial distortion, and decentering distortion [4, 7]. The values that define the modeling of these effects, along with the focal length, are called internal camera parameters and are generally solved for with a calibration method. It is important to note that internal camera parameters are often highly dependent on the lens settings such as zoom and focus.

Principal point shift is caused by a misalignment of the lens with respect to the image plane. The other distortion parameters are measured with respect to the location of the principal point, and so it must be accurately known in order to achieve optimum model results. However, adjusting other internal and external parameters to compensate for an unknown principal point location has been shown to produce acceptable results [8]. The principal point shift is accounted for by replacing the  $x$  and  $y$  coordinates with adjusted values  $x - x_0$  and  $y - y_0$ , where  $x_0$  and  $y_0$  are the location of the principal point.



Radial distortion is an increase or decrease in magnification based on radial distance from the principal point. It contributes to what is known as “barrel” and “pincushion” effects shown in Figure 2.2. Radial distortion can be modeled as a polynomial function of the radial distance  $r$

$$dx = k_1 x r^2 + k_2 x r^4 \quad (2.8)$$

$$dy = k_1 y r^2 + k_2 y r^4 \quad (2.9)$$

$$r^2 = x^2 + y^2 \quad (2.10)$$

where internal camera parameters  $k_1$  and  $k_2$  define the extent of the distortion. For wide angle lenses it may be necessary to extend the radial distortion polynomial with a sixth order term [9]. Other formulations of the distortion polynomial include using odd powers of radial distance instead of even [5].

Decentering distortion is caused by misalignment of the lens. An example of its effect on image points can be seen in Figure 2.3. It can be modeled and corrected for as shown in Equation 2.11 and 2.12

$$dx = p_1(r^2 + 2x^2) + 2p_2xy \quad (2.11)$$

$$dy = p_2(r^2 + 2y^2) + 2p_1xy \quad (2.12)$$

where internal camera parameters  $p_1$  and  $p_2$  define the extent of the distortion. Decentering distortion is a less significant effect, being usually an order of magnitude less than radial distortion[10].

The extended model can be written as

$$M \begin{bmatrix} X - X_L \\ Y - Y_L \\ Z - Z_L \end{bmatrix} = \frac{1}{k} \begin{bmatrix} x - x_0 + dx \\ y - y_0 + dy \\ -f \end{bmatrix} \quad (2.13)$$

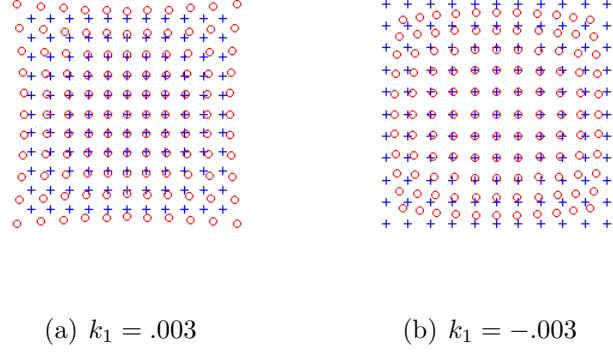


Figure 2.2: Effect of pincushion (a) and barrel (b) radial distortion on image points. Crosses represent undistorted points and circles show the effect of distortion

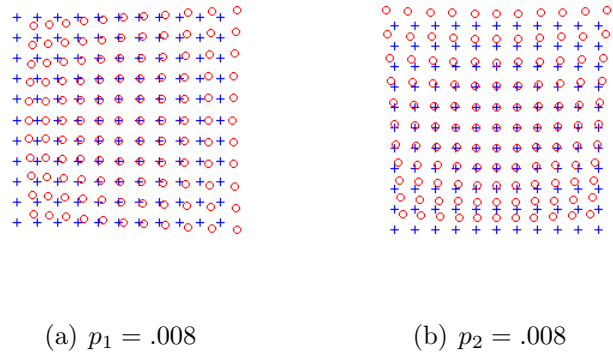


Figure 2.3: Effect of decentering distortion on image points. Crosses represent undistorted points and circles show the effect of distortion

where

$$dx = k_1(x - x_0)r^2 + k_2(x - x_0)r^4 + p_1(r^2 + 2(x - x_0)^2) + 2p_2(x - x_0)(y - y_0) \quad (2.14)$$

$$dy = k_1(y - y_0)r^2 + k_2(y - y_0)r^4 + p_2(r^2 + 2(y - y_0)^2) + 2p_1(x - x_0)(y - y_0) \quad (2.15)$$

Other distortion parameters can be found in the literature as well. Gruen [5] includes scaling and shear corrections to compensate for imprecisions introduced by the image sensor and image acquisition technique; however Remondino and Fraser [11] state that such corrections are rarely significant in modern digital cameras.

*2.1.3 Camera calibration.* A calibration procedure is performed to determine the internal camera parameters discussed above, and there are several methods. Images can be taken of a regularly spaced point cloud such as a calibration-grid, and the camera parameters are solved for along with the point locations during bundle adjustment. This method does not require the grid measurements to be known beforehand, but does need to be performed separately before beginning a measurement project. Alternatively, calibration can be performed simultaneously with project data generation. The computational process is identical to the previous method, but project points and image angles are constrained by the requirements of data collection and the project environment, and this can lead to less robust configuration for the bundle adjustment process. Remondino and Fraser [11] provide a good discussion of the relative merits of different calibration techniques.

Because of the convenience and usefulness of zoom lenses, a significant amount of research has gone into methods of calibration for these systems. The intrinsic camera parameters are dependent on lens settings on focal length and focus, and so means of determining the parameters are needed that are practical and produce satisfactory results. Willson [12] provides an in-depth look at pan-tilt-zoom camera calibration, and suggests a bivariate polynomial interpolation of the focal length, principal point and  $k_1$  distortion parameter with respect to zoom and focus settings, based on sets of calibration data at many lens positions. More recently, Fraser and Al-Ajlouni [10] described a more

practical method for use with inexpensive digital cameras. Their results showed a linear interpolation of the photogrammetric focal length, principal point, and  $k_1$  distortion parameter based on the camera focal length setting was sufficient for object accuracy on the order of 1:10,000 (one unit error for 10,000 units object length).

Fraser and Al-Ajlouni describe the convenience of using zoom lenses for taking photogrammetrically suitable images of architectural and historical sites, traffic accidents and other applications. The measurement system proposed in this thesis makes use of zoom lenses for keeping the test object well framed in each image as it moves around the capture volume. A similar approach to those taken in the papers described above will be used to generate a continuum of calibration parameters based on the settings of the lenses at the time each image is taken. The use of curve fit calibration parameters for processing a sequence of images taken at changing lens settings has not been found in the literature by this author.

*2.1.4 Videogrammetry.* Videogrammetry operates on the same principles as photogrammetry, but applies to a series of image sets. The result is a time history of three dimensional point data from which kinematic or vibrational information can be extracted. Because of the number of image sets to be processed, videogrammetry systems will often include methods that reduce processing time and increase automation, especially in the process of feature recognition. Processing using texture-based methods usually requires intelligent application of filters and constraints or precise test setup, and therefore can be very labor intensive. Discrete targets are often employed instead to allow automatic marking and referencing of points between images and epochs [13–17]. Further robustness can be achieved by using a light source, cameras filtered for a specific wavelength, and retroreflective markers [18]. The markers produce high contrast points in images which lend themselves to filtering of extraneous data.

Real-time videogrammetry systems are the extreme case of automated photogrammetry processing. Real-time systems can generate three-dimensional data at periods on the order of milliseconds at frame rates of 120Hz and higher [18]. Target data can be matched to a library of object marker patterns and the location and orientation of an

object can be found. Fast processing is aided by using retroreflective markers and by calculation of the interior and exterior camera parameters prior to image collection. Advances in subpixel marking techniques including the use of greyscale data for calculating the centroid of targets has greatly improved the accuracy of these systems.

#### *2.1.5 Applications of photogrammetry to membrane structures measurement.*

Photogrammetry has several characteristics that make it attractive as a noncontact measurement tool:

1. It is relatively inexpensive, and satisfactory results can be obtained with off-the-shelf hardware.
2. It is adaptable to a wide variety of environments.
3. It has typical accuracies on the order of 1/10th of a pixel
4. Data are captured at all points simultaneously.
5. Image data can be stored for reference and (additional) processing at any time.

For these reasons, it is being adopted in a wide variety of fields. Recent research has gone into developing benchmarks and best practices for photogrammetric measurement of specific kinds of surfaces [6, 13, 19]. In fields such as MAV aerodynamic research, photogrammetry has become the standard measurement technique for structures such as flapping wings [20–22].

The use of photogrammetry to measure large space structures has been steadily developing over the past ten years. Pappa et al. [23] described in a 2001 paper the use commercially available cameras and software to derive the surface profile of a 5 m inflatable antenna. Retroreflective targets were used along with flash photography to create defined targets on the structure, and results showed an accuracy on the order of 1:10,000. Blandino et al. [13] investigated the use of videogrammetry for modal identification in membrane structures and compared the results with those from scanning laser vibrometer. Pappa et al. [14] investigated laser dot projection of targets onto the membrane structure to maintain high target contrast without the use of physically attached retroreflective targets, and Dorrington et al. [1] used fluorescent coatings to

generate targets on transparent membranes. More recently, videogrammetry has been used to measure in-plane motion of a thin film [15].

Photogrammetry has also been used extensively as a measurement tool in MAV research. Lightweight and flexible materials are often critical design components, and it would be difficult or impossible to attach physical sensors without affecting their dynamic response. Pitcher et al. [16] gives an analysis of the mode shapes of the wing of a Nighthawk mini-UAV at various angles of attack. Three synchronized cameras captured images at 75 frames per second of the Nighthawk in the wind tunnel. The wing of the nighthawk was covered with a combination of coded and uncoded targets and additional targets were placed on the floor around the vehicle for reference. Results showed that the videogrammetry system was well-suited to measuring the large displacements of the wing, but the limited resolution of the system, approximately .5mm per pixel, meant low-amplitude wing vibration was lost in noise. However, at test conditions that did produce large enough displacements, power spectral density curves were generated and animation of the vibration of the wing at resonant frequencies was accomplished.

Photogrammetry techniques have become the standard for wing shape measurement of flapping wings. Curtis et al. [20] analyze the shape of a number of wings of different shapes and materials by taking synchronous images of a laser dot pattern projected onto the surface of the wing while it flaps on a test stand. Additional printed dots were fixed to the flapping mechanism for reference. The images are processed using PhotoModeler<sup>1</sup> photogrammetry software, and a time history of the surface shape was generated. This method had the advantage of minimal interference with the structure of the wing being tested, since no physical targets were attached to the wing surface. A denser profile can be obtained with a digital image correlation (DIC) method, a texture-based photogrammetry technique, as described in Aono et al. [21] and Chakravarty and Albertani [22]. A random speckle pattern is applied to the test article and is correlated between synchronous images. Aono et al. used stereo high speed cameras to capture images of a flapping wing in a vacuum chamber. Chakravarty and Albertani examined the membrane alone, mounted on a wire ring, undergoing static and dynamic deforma-

---

<sup>1</sup>Eos Systems Inc. 210 - 1847 West Broadway Vancouver, BC V6J 1Y6

tions. Both systems perform temporal tracking, which correlates the speckle pattern across epochs.

All techniques used in MAV wing shape and space structure measurement currently require the test article to be on a stand or actuator and the cameras and other photogrammetry equipment placed around it. This tends to restrict the kind of testing that can be performed on the article to cruise and hovering flight conditions in the case of MAVs and fixed-average-position tests for both MAVs and membranes. Measurement of wing shape during maneuvering flight has not been found in the literature by this author, nor has deploying or translating membranes. Expanding the use of photogrammetry to include such test conditions will provide unique data sets for improved understanding of the characteristics of these structures.

Real-time videogrammetry is widely used to rapidly prototype automatic control strategies. By moving location sensing off-board the vehicle, complex control strategies can be tested on inexpensive vehicles, thereby eliminating the costs of a lightweight implementation on the vehicle and the risk of damage in the case of a vehicle crash. Massachusetts Institute of Technology’s Real-time indoor Autonomous Vehicle test Environment (RAVEN) [24] and Boeing’s UAV Swarm testbed [25–27] host tests ranging from cooperative control of vehicles to nonlinear control for aircraft aerobatic maneuvers. These systems require many cameras for maximum redundancy. These systems are popular for post-processing applications as well, in the entertainment industry, in biometric analysis, and inverse kinematics [28]. Though other efforts have been made at close-range object location and orientation, real-time videogrammetry systems are the most widely accepted. [29–31]

## ***2.2 Comparison with Other Noncontact Measurement Systems***

Comparison of photogrammetry to other noncontact measurement systems helps to illustrate the strengths and weaknesses of the technique. Laser vibrometry has been an accepted measurement tool for many years, and is often used as a control measurement in investigations of new measurement techniques [13]. 3-D time-of-flight laser scanners share similar properties to laser vibrometers, but measure static three dimensional po-

sition rather than velocity. Other measurement systems such as Moire interferometry, geometric Moire, and capacitance measurement have been used, especially for the measurement of membrane structures.

Laser vibrometry is the measurement of velocity of an object based the interference of a laser beam with the reflected response from an object. Based on the phase shift in the light due to the Doppler effect, relative velocity of the object can be calculated directly. Laser vibrometry is a point-based measurement device which takes data at specific locations on an object. An entire surface can be analyzed by collecting data over a grid of points. Data can be recorded at frequencies of a MHz and higher and with micrometer resolutions. As noted above, videogrammetry measurements have data collection rates limited by the frame rates of the cameras used, and systems exceeding several hundred fps are rare.

The high measurement frequency and and resolution of laser vibrometers come at a cost. As is noted in [13], laser vibrometry is a relatively expensive technology compared to videogrammetry, with single-point vibrometry systems starting at \$20,000 and scanning systems costing over \$100,000. The performance benefit does not always justify the additional cost in applications such as large space structures, where vibration frequencies are often quite low. Also, Pitcher et al. [16] notes that large amplitude vibrations are often well above the maximum threshold of laser measurement systems. In photogrammetric systems, the amplitude of the measurements is limited by the depth of field of the cameras being used, and in most cases, this is quite large in comparison to laser vibrometers.

3-D time-of-flight laser scanning measures three dimensional locations, and shares some of the characteristics of laser vibrometers in that it is not affected by ambient lighting, and records data point by point. Markley et al. [2] describe this measurement technique as it relates to modeling of as-built facilities and note that in practice its accuracy is comparable to photogrammetry, but that it is much less time consuming than photogrammetry to initially gather data when analyzing large structures. Generating models from the data from either measurement technique can be labor intensive and



prone to operator error. A hybrid technique was suggested as a way of overcoming the limitations and providing redundancy.

Moire interferometry has the benefit of being a full field measurement technique, but requires a diffraction grating or grid to be attached to the test object. Other interferometry techniques do not require surface preparation, but all need a generally flat surface and relatively low displacement [32]. Capacitance measurement is also found in the literature but is not common and requires a flat, conductive surface [33].

In summary, photogrammetry is the preferred option in situations that require versatility and a moderate degree of accuracy. Its full-field capability as well as its ability to self-validate its data are useful properties in many applications. As imaging technology improves, photogrammetry will continue to get more accurate and reliable.

### ***2.3 Hybrid Measurement Systems***

The term “hybrid measurement system” refers to the combination of two or more measurement systems to accomplish a single task. There are two senses in which the systems are combined: data merging and system slaving. Data merging, which is far more common in the literature, is the combining of data gathered from two different measurement systems in order to provide redundancy and to compensate for deficiencies in the individual data sets [2, 34, 35]. System slaving is the controlling of one local measurement system with another global measurement system. This method is useful when there is one particular area of interest that could be at an arbitrary location in large volume.

The concept of master-slave system relationship for sensors is used in the area of surveillance camera networks, in which a wide-angle camera directs a pan-tilt-zoom camera to a location of interest such as a person [36, 37]. The purpose of these systems is to provide clear images that allow a person’s biometric characteristics to be identified by an operator. Strictly speaking these systems should be distinguished from measurement systems, since precise quantitative data is not required on the object of interest.

Slaving of measurement systems is a new area of study begun three years ago at the Air Force Institute of Technology. A hybrid system was developed which involved a real-time videogrammetry system for detecting the global location and orientation of an object, and a mirror system to direct a laser vibrometer beam onto a point on the object [38, 39]. The static and dynamic error of the aiming system was determined and vibrational data of a moving object was shown to correlate with a static object case. The major deficiency of the system was the time delay involved in calculating the coordinates of the object by the videogrammetry system and transmitting the data to the laser steering system. The delay of approximately 200 ms caused the laser to point at a previous location of the object and therefore limited the speed at which the object could be moved and still have the laser illuminate it. The tracking error was improved with the addition of a Kalman filter to the tracking algorithm, but the fact that laser vibrometry is a point measurement technique still presented difficulties. The use of photogrammetry as the local measurement system will help to resolve this difficulty, since it is a full-field measurement technique.

This research combines a real-time videogrammetry system for detecting global location of the test object and four PTZ cameras for taking high-speed, high-resolution images suitable for photogrammetry. In the next section, the details of the system design will be presented, including system configuration, the determination of the gimbal and lens settings, and the software controller.

### III. System Design and Development

#### 3.1 System Overview

The dynamic tracking and measurement (DTM) system consists of two hybridized subsystems:

1. A videogrammetry system to capture large scale 3D motion.
2. A set of synchronized pan-tilt-zoom (PTZ) cameras that can capture motion at high frame rates.

The videogrammetry system calculates the position of the object in real time using the retroreflective markers placed on the object. The object coordinates are passed to software controllers which calculate gimbal azimuth and elevation and lens zoom and focus for each PTZ camera. Images are captured synchronously at up to 500 fps and stored on the controller computers. Testing equipment includes a rotating table used to constrain dynamic motion. Each component is coordinated as needed through hardware and software interfaces. A block diagram of the hybrid system is shown in Figure 3.1, the videogrammetry camera setup is shown in Figure 3.2. A PTZ camera is shown in Figure 3.3 with the rotating table in Figure 3.4.

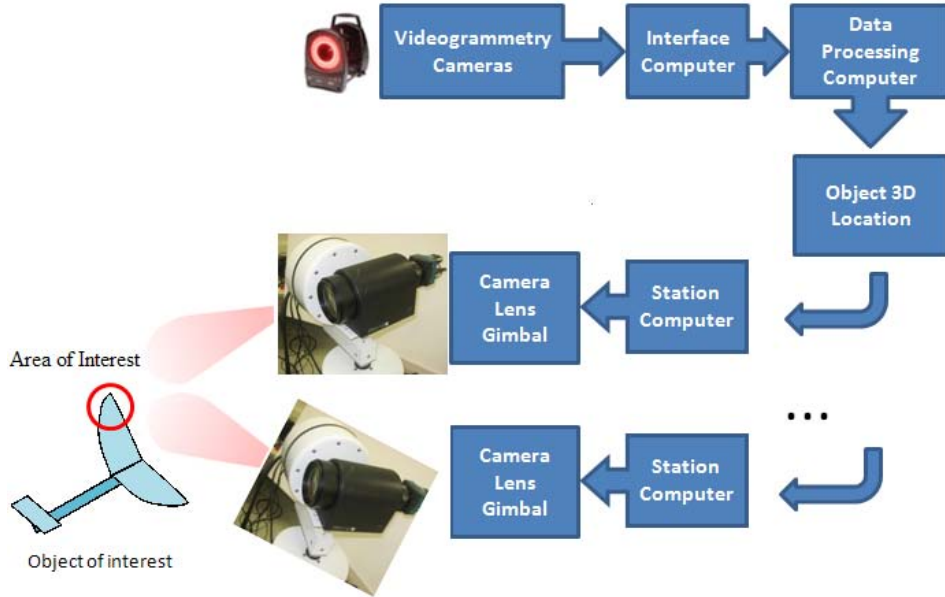


Figure 3.1: The DTM system consists of a videogrammetry subsystem for real-time motion capture and four pan-tilt-zoom camera subsystems.

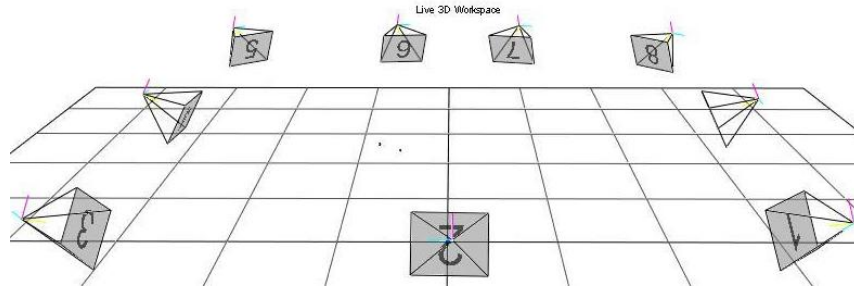


Figure 3.2: Videogrammetry cameras are setup around the room's perimeter and track body motion. Each tracking subsystem uses this data to focus at the moving point.



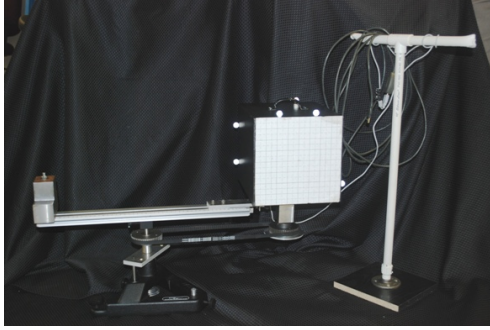
Figure 3.3: A camera subsystem consists of a two axis gimbal, zoom-focus lens, a high speed camera, and controller computer (not shown).

### 3.2 Videogrammetry System

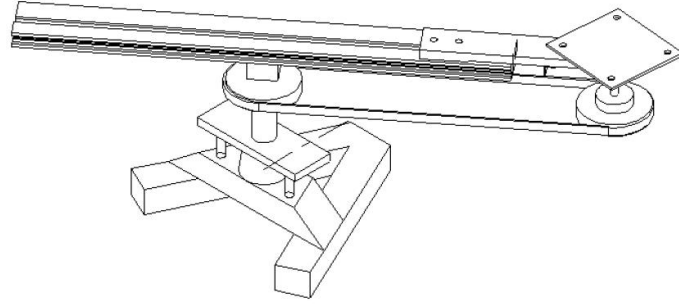
Three dimensional position measurement of an object of interest is accomplished by a videogrammetry system built by Vicon<sup>1</sup>. Ten cameras are mounted around the lab perimeter<sup>2</sup> (see Figure 3.2). Retro-reflective spherical videogrammetry targets imaged by cameras are marked to subpixel accuracy. The 2-D locations of marked targets on each image are then sent to the central data station which interprets them as rays through space. Knowing each camera's location and orientation, the global location of the markers is determined by ray intersection to determine a 3-D location in the videogrammetry coordinate system (VCS). Sets of 3-D global target positions are compared to a library

<sup>1</sup>Vicon, 5419 McConnell Avenue, Los Angeles, CA 90066, USA [moveme@vicon.com](mailto:moveme@vicon.com)

<sup>2</sup>The videogrammetry cameras are MX T160 type with 16 megapixel resolution. Software used was Tracker v1.1. The working capture volume is approximately 5m x 7m x 2.5m. Markers of 3mm-8mm diameter were used.



(a) Turntable showing mounted videogrammetry object



(b) Turntable detail

Figure 3.4: Samples can be mounted on a platform that maintains orientation while moving through a circular path.

of objects. For each pattern match, the location and orientation of its body coordinate system is determined with respect to the global coordinate system.

The videogrammetry system must be calibrated prior to use, after re-orienting the cameras, and after normal disturbances have affected the camera positions sufficiently. The system is calibrated by using a specially designed videogrammetry object called a calibration wand, shown in Figure 3.5. The wand is moved about the volume and a number of frames, typically 2500, are recorded by each camera. The frames are processed, and the root-mean-square (RMS) error for individual camera rays are calculated to provide insight on the quality of the calibration. Typical RMS error values range from .25 mm to .35 mm. The origin of the VCS is set by placing the calibration wand at the desired location and recording it in the software.

The noise of the position measurement was characterized by the perceived motion of a stationary object. Translation on the order of 0.75 mm and rotation on the order of  $0.005^\circ$  were observed; both well below the requirements for centering an object in the field of view. Similar results were obtained in Ref. [18]. The videogrammetry system has an update rate of 120 Hz at full field resolution.

Objects are defined in Vicon by selecting a collection of retroreflective markers affixed to the object and assigning them a unique identifier. The markers must be placed sufficiently nonsymmetrically to allow the software to determine orientation, and the pattern must distinguishable from other defined objects. Spherical markers are



Figure 3.5: Calibration wand used to calibrate and set the origin of the videogrammetry system

the most robust, since they appear identical from any direction, but two-dimensional circles of retroreflective tape can also be used, provided that the viewing angle of the videogrammetry cameras is not too shallow.

### 3.3 Camera Gimbals

Each PTZ camera is steered by a gimbal (shown in Figure 3.3) which rotates about perpendicular axes. The bottom servo rotates for panning (also known as azimuth) and the top servo rotates for changing elevation. Elevation and azimuth command messages are sent by serial communication to the gimbal which interprets and returns its current position. The nominal position accuracy is  $0.01^\circ$  and maximum slew rate is  $120^\circ$  per second.

*3.3.1 Camera aiming.* The gimbal control software calculates the azimuth and elevation angles for accurately aiming the camera. Assume that the location and orientation of the gimbal system are known and given by a position  $\vec{p}$ , and unit vectors for the body  $x$ ,  $y$  and  $z$  axes,  $\vec{a}$ ,  $\vec{b}$  and  $\vec{c}$  respectively and that the location of interest is  $\vec{q}$  with all vectors given in the VCS. The point  $\vec{p}$  lies at the intersection of the azimuth rotation axis and the elevation rotation axis. The gimbal body coordinate system (BCS)  $z$  axis is collinear with the azimuth axis and the body  $y$  axis is collinear

with the elevation rotation axis at home position. The directions are chosen so that the system is right handed and  $x$  points out parallel to the camera's optical axis. This axes definition ensures that tracking angles correspond to counterclockwise rotations about the respective axes. Figure 3.6 illustrates the coordinate systems and their relationships.

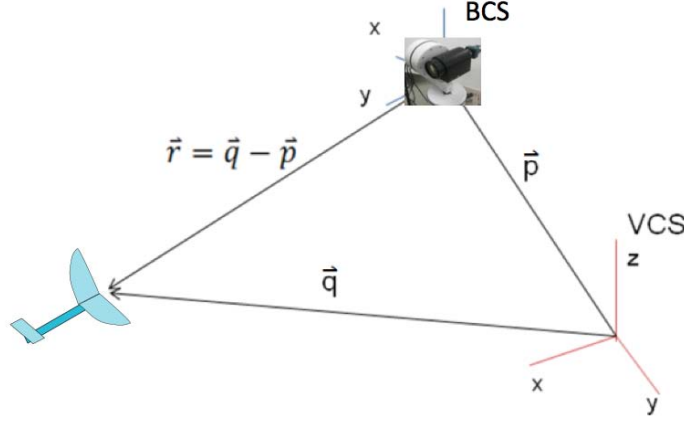


Figure 3.6: Vector  $\vec{r}$  is the distance between the gimbal and test object, and is transformed into gimbal body coordinate system to calculate azimuth and elevation angles.

The vector  $\vec{r} = \vec{q} - \vec{p}$  represents the line connecting the camera to the point of interest. The transform  $(\vec{r}^\top [\vec{a}, \vec{b}, \vec{c}])^\top = \vec{r}'$  gives the line in BCS. The elevation angle,  $\psi$ , is found by

$$\psi = \arctan2 \left( \vec{r}'_z / \sqrt{\vec{r}'_x^2 + \vec{r}'_y^2} \right) \quad (3.1)$$

where  $\arctan2$  is the inverse tangent that uses the signs of the numerator and denominator to distinguish quadrant. The azimuth angle,  $\phi$ , is found by

$$\phi = \arctan2 \left( -\vec{r}'_y / \vec{r}'_x \right). \quad (3.2)$$

**3.3.2 Camera location.** In order to calculate azimuth and elevation angles, the gimbal BCS must be known in relation to the VCS. The following section describes several methods of determining the BCS. The BCS can be located by hand, by photogrammetry, or by being defined and located by the videogrammetry system. Each method has advantages and disadvantages which will be discussed.

Hand location is any method that locates the BCS by manually adjusting the location and orientation parameters. This can be as simple as using a tape measure to find the  $x$ ,  $y$  and  $z$  coordinates and aligning the BCS and VCS orientation. However, another hand method was developed that isolates the coordinates and allows them to be adjusted individually, and is described next.

The three orientation parameters which define the BCS orientation can be reduced to one  $z$  axis rotation by ensuring the gimbal is mounted on a flat surface or level tripod as shown previously in Figure 3.3, so that the  $z$  gimbal axis is aligned with the VCS  $z$  axis. A step-by-step method was developed for determining the three location coordinates and  $z$  axis rotation one at a time. The rotation angle about the  $z$  axis,  $\theta$ , is found by tasking the camera to point along the BCS  $x$  or  $y$  axis. The VCS  $x$  and  $y$  axis are easily visible on the lab floor, and  $\theta$  is adjusted until the camera is observed to be pointing along the corresponding VCS axis. The  $z$  coordinate is found by holding a videogrammetry object at the same height as the camera, and reading the  $z$  coordinate of the object. The  $x$  and  $y$  coordinates are found in a two step process, illustrated in Figure 3.7. First, a videogrammetry object is placed along either the  $x$  or  $y$  axis, and the tracking system is tasked to point at where it thinks the object is based on the current estimated camera location. The other location parameter is adjusted until the camera is pointing at the object. Second, the object is moved off the axis and the final parameter is adjusted until the camera points at the object.

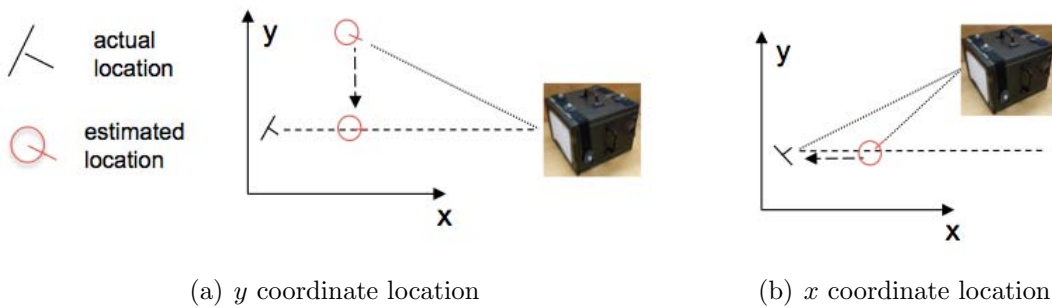


Figure 3.7: Videogrammetry object is aligned with  $x$  axis and  $y$  camera coordinate is adjusted, then the object is moved off-axis and the  $x$  coordinated is adjusted.



The method described above produces camera locations that are adequately accurate for tracking objects in motion in the lab. The BCS location can be found to within approximately 2.5 cm in each axis direction. Finer adjustments than this produce no gain in aiming accuracy over the capture volume, due to errors in the  $z$  axis orientation and camera mounting. There are several drawbacks to this method. The method must be repeated for each camera location, which is time-consuming. Furthermore, the possible location of the cameras are restricted by the capture volume. The camera height cannot be measured if it is mounted higher than the maximum height the videogrammetry system can detect an object. Therefore, a more versatile method has been developed that would overcome some of these problems.

The new method uses the videogrammetry system and PhotoModeler photogrammetry software to find the locations and orientations of all cameras at the same time. This method requires knowing the internal calibration parameters for each camera in order to perform accurate photogrammetric processing. The photogrammetry processing generates the location and orientation of the cameras with respect to an arbitrary coordinate system when it performs the bundle adjustment on a set of images. By transforming these coordinates into the VCS, the proper camera parameters can be found.

To help with this process, a special targeted object is used, shown in Figure 3.8. This targeted object has retroreflective videogrammetry markers and PhotoModeler coded targets on it. The purpose of the object is to allow the videogrammetry object coordinate system (VOCS) and the photogrammetry coordinate system (PCS) to be defined identically. This reduces the number of coordinate transformations and reduces error. The axes and scale attached to the targeted object are defined with a set of images of the object before taking images for camera location. Any calibrated camera can be used for setting up the targeted object.

The videogrammetry object is defined such that the origin of the VOCS is located at one of the retroreflective markers, the  $x$  axis aligned with another marker, and the  $y$  axis in the plane of a third. The coded targets are used to speed up image processing by allowing automatic marking and referencing. A set of images are taken with a calibrated camera, and a flash is used to cause the retroreflective markers to show up brightly. The

coded targets are automatically marked and referenced by the photogrammetry software, and the high-contrast retroreflective markers are marked and referenced by hand using the software's subpixel marking tool. The images are processed to generate the three-dimensional coordinates of each referenced point. Since the retroreflective markers were referenced, these points can be used to define the PCS the same way as the VOCS was defined.

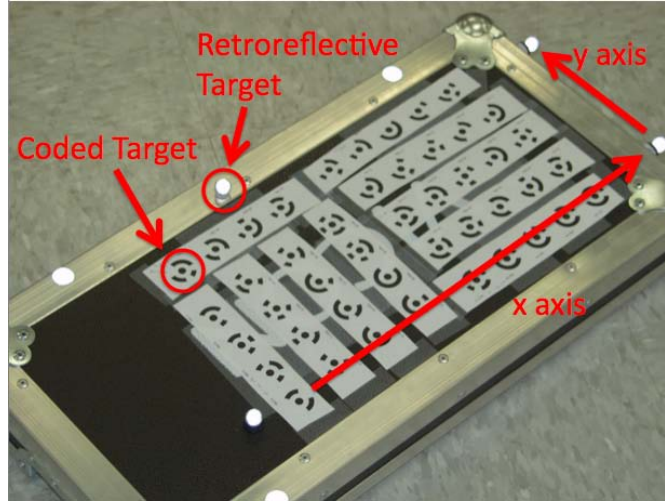


Figure 3.8: Targeted object used for camera location. Retroreflective and coded targets are shown. The VOCS and PCS  $x$  and  $y$  axes are shown, with the origin at their intersection and the  $z$  axis oriented so as to form a right hand coordinate system.

The photogrammetry project and the images used to set up the targeted object are duplicated and reused for every new camera location project. The targeted object will only need to be redefined if either the retroreflective markers or coded targets are changed or disturbed. Therefore it is important that they be securely attached to the object.

Once the targeted object is defined, it can be used to locate the PTZ cameras. This can be done one at a time or in groups, the limiting factor being the ability of each camera to see the coded targets on the targeted object. An additional restriction is that the internal parameters of each of the PTZ cameras must be known. These can be determined from a calibration at the current camera state, or by approximating the parameters using curve fits to a set of calibrations. Curve fit calibration parameters will be described in a later section. The most important parameter for camera location is

the focal length. It was found to be difficult to get the required accuracy for camera location with a curve fit approximation, and the best results have been obtained by using a camera state at which the camera calibration routine has been run.

The targeted object is placed in a location where each camera can see it. The location and orientation of the targeted object in the VCS is recorded, and images of the targeted object are taken with each camera. If desired, the targeted object can be rotated and additional sets of images, locations and orientations can be gathered to provide redundant locations for error checking. The images are imported into the PhotoModeler project set up previously, and they are automatically marked and processed using the internal camera parameters. The processing generates camera locations and orientations in the PCS.

The final step is to transform the PCS locations and orientations into VCS. The PCS locations,  $[x_p, y_p, z_p]^\top$ , are transformed by multiplying by a rotation matrix derived from the orientation of the targeted object in VCS, defined by body 1-2-3 angles  $\phi_v$ ,  $\theta_v$ , and  $\psi_v$ , and adding it to the translation vector from the VCS origin to the targeted object,  $[x_v, y_v, z_v]^\top$ .

$$\begin{bmatrix} x_c \\ y_c \\ z_c \end{bmatrix} = \begin{bmatrix} x_v \\ y_v \\ z_v \end{bmatrix} + C_{pcs,vcs} \begin{bmatrix} x_p \\ y_p \\ z_p \end{bmatrix} \quad (3.3)$$

where  $C_{pcs,vcs}$  is the rotation matrix from PCS to VCS given by

$$C_{pcs,vcs} = \begin{bmatrix} \cos(\psi_p) & -\sin(\psi_p) & 0 \\ \sin(\psi_p) & \cos(\psi_p) & 0 \\ 0 & 0 & 1 \end{bmatrix} \begin{bmatrix} \cos(\theta_p) & 0 & \sin(\theta_p) \\ 0 & 1 & 0 \\ -\sin(\theta_p) & 0 & \cos(\theta_p) \end{bmatrix} \begin{bmatrix} 1 & 0 & 0 \\ 0 & \cos(\phi_p) & -\sin(\phi_p) \\ 0 & \sin(\phi_p) & \cos(\phi_p) \end{bmatrix} \quad (3.4)$$

This transformation gives the location of the camera in VCS,  $[x_c, y_c, z_c]^\top$ , which can be directly entered into the tracking controller.

Since we have assumed that the PTZ camera  $z$  axis is aligned with the VCS  $z$  axis, there is only one camera rotation parameter to find, the rotation about the  $z$  axis,  $\theta$ . The camera coordinate system (CCS) in PCS is given in body 1-2-3 form, with the camera  $x$  axis pointing to the right of the image plane and  $y$  axis pointing up, if looking at the camera from behind (illustrated previously in Figure 2.1). The  $z$  axis lies along the optical axis pointing the opposite direction of the camera. Thus the negative  $z$  axis points out the front of the lens. A rotation matrix  $C_{ccs,pcs}$  can be formed from the rotation angles  $\phi_p$ ,  $\theta_p$ , and  $\psi_p$ , and multiplying this by the rotation matrix from PCS to VCS gives the camera orientation in VCS. The unit vector passing through the front of the lens is given by

$$\begin{bmatrix} \hat{x} \\ \hat{y} \\ \hat{z} \end{bmatrix} = C_{pcs,vcs} C_{ccs,pcs} \begin{bmatrix} 0 \\ 0 \\ -1 \end{bmatrix} \quad (3.5)$$

The angle  $\theta$  is found by subtracting the angle between the projection of the vector out the front of the lens onto the VCS  $x$ - $y$  plane and the VCS  $x$  axis from the gimbal azimuth angle. First evaluate the cross product of the projection of the camera ray on the VCS  $x$ - $y$  plane and the  $x$  axis.

$$\vec{w} = \begin{bmatrix} \hat{x} \\ \hat{y} \\ 0 \end{bmatrix} \times \begin{bmatrix} 1 \\ 0 \\ 0 \end{bmatrix} \quad (3.6)$$

The angle between the two vectors is given by

$$\theta' = \arcsin \left( \frac{|\vec{w}|}{\sqrt{\hat{x}^2 + \hat{y}^2}} \right) \quad (3.7)$$

Subtracting  $\theta'$  from the gimbal azimuth angle at which the photograph was taken gives the desired rotation value  $\theta$ .

These transformations are performed in a MATLAB script which has as inputs the VCS and PCS data and outputs the camera location parameters and the angle  $\theta'$  of the

camera.  $\theta'$  must be subtracted from the gimbal azimuth angle manually to determine the  $\theta$  parameter.

To test the effectiveness of this method of locating the cameras, twenty camera locations were generated based on three separate projects. During project one and two, the PTZ camera was mounted on a tripod about 1.5 m off the floor and about 3 m from the center of the room and the targeted object was placed on the floor in the center of the room. During project three, another camera was included to illustrate the process of locating more than one camera at the same time. The VCS origin was defined to be in the center of the room but at table height, approximately 0.6 m above the floor.

The PTZ camera was calibrated at the lens settings that were used for image capture. The lens settings were not changed between projects. Images were captured of the targeted object during each of the first two projects. The targeted object was rotated between each image, and the videogrammetry coordinates of the new location was recorded each time. The PTZ camera orientation was not changed. The set of images was imported into a PhotoModeler photogrammetry software project which included the “set-up” images which were used earlier to define the PCS. The photos were processed, and the locations and orientations of the camera in the PCS were exported. This data, along with the location of the targeted object in each image, were imported into the MATLAB script and the transforms described above were applied.

Project three was processed in an identical way, except an additional PTZ camera took images at each of four targeted object positions. In order for the object to be in view of both cameras, the object was moved from the center of the room and the orientations, but not location, of the PTZ cameras was changed from project one and two.

The data from each project for the primary PTZ camera is shown in Table 3.1. Listed is the standard deviation in each direction, and the distance that the average of all generated locations were from the hand location method. Even considering the uncertainty of the hand location method, approximately 2.5 cm in each direction, the average value is consistently outside this. This makes intuitive sense, since the photogrammetry method of location measures from the ideal focal point of the lens, which does not coincide with the origin of the gimbal axes. In other words, the origins of the CCS and the

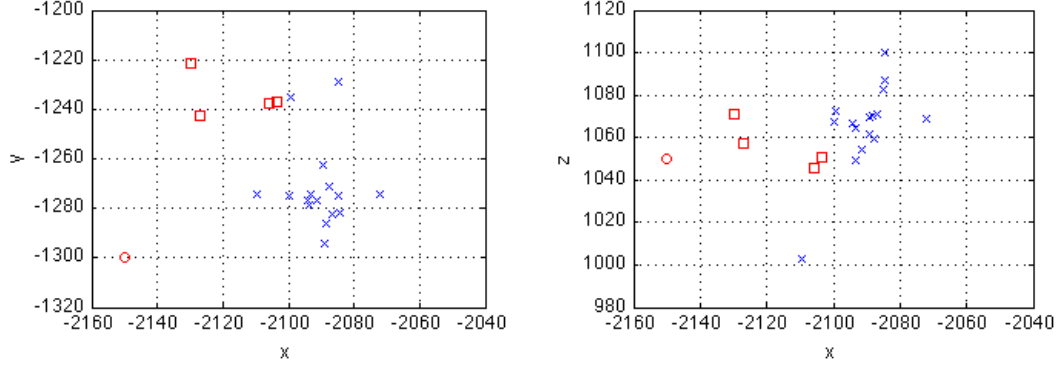
gimbal BCS do not in general coincide. This fact illustrates the principle deficiency of location of the cameras by this method. There is currently no simple way to relate the focal point to the origin of the gimbal axes.

Figure 3.9 shows the camera locations generated by the photogrammetry method and the hand-generated gimbal location. It can be seen that the photogrammetry-generated locations are generally located closer to the object than the hand-generated locations. Also, project three data are rotated counterclockwise around the control point, corresponding to the rotation of the camera for that project. Thus the data appear to roughly lie on the optical axis of the camera ahead of the gimbal origin (see Figure 3.10). It is supposed that with additional data, a correction factor could be derived that would account for the error, considering that the data are generally precise. In particular, additional data should be gathered on the dependence of the generated locations on the lens settings. Focal length and focus setting may have a significant effect on the position of the ideal focal point.

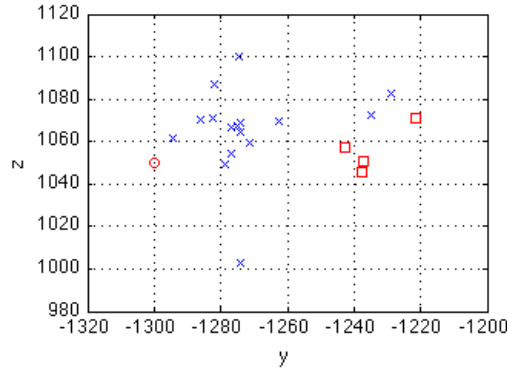
It was found that the photogrammetry method of locating the cameras was precise but less accurate than the hand calibration method. Although highly accurate location of the cameras is not necessary, deviations over 5 cm produce noticeable aiming errors which could result in lost image data. Potential benefits of multi-camera location are currently outweighed by the need to calibrate the cameras prior to use. If improved curve fits to the calibration parameters are developed which would obviate the need for pre-calibration, as well as a correction factor for the difference between focal point and gimbal origin, this method may become useful for large multiple-PTZ-camera systems where the cameras are located outside the capture volume.

Table 3.1: Data from camera location by photogrammetry

Project	Images	$\sigma_x$ (mm)	$\sigma_y$ (mm)	$\sigma_z$ (mm)	Dist. of average from hand location (mm)
1	8	8.11	4.45	7.39	65.6
2	8	8.93	23.35	28.98	70.2
3	4	13.88	9.01	10.95	73.7
All	20	14.05	21.73	19.25	66.4



(a)  $x$ - $y$  graph of approximated camera locations (b)  $x$ - $z$  graph of approximated camera locations



(c)  $y$ - $z$  graph of approximated camera locations

Figure 3.9: Planar graphs of camera locations with respect to hand location point (denoted by circle). Blue  $x$  denotes project one and two points. Red square denotes project three points, found after rotating camera. Scale is in millimeters.

A third camera location technique involves using retroreflective videogrammetry targets to register the gimbals as videogrammetry objects, with their origin at the gimbal axes intersection. This is the most direct approach to camera location; since the goal is to know the camera locations in the VCS, it makes sense to have them located by the videogrammetry system. Furthermore, once the gimbal videogrammetry objects are defined, there is very little additional work for the operator. The camera stands can be moved to a new location and the videogrammetry system will record the location and pass it to the aiming software automatically. However, this method requires that the cameras be placed within the capture volume of the videogrammetry system, and therefore reduces the amount of the volume that can be used for test articles. This can

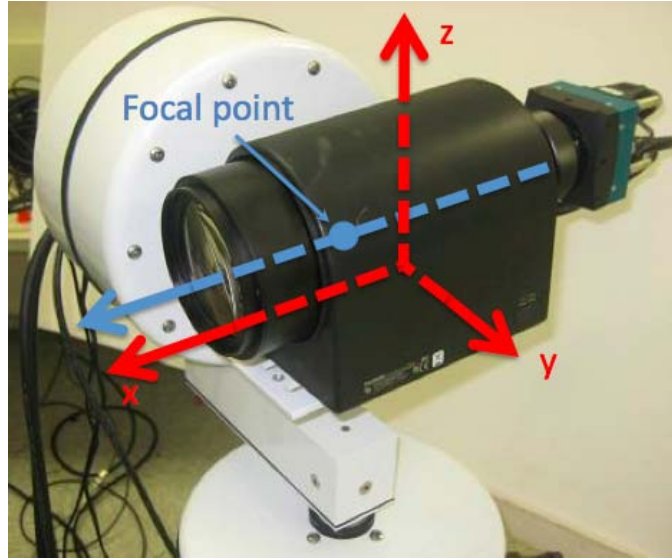


Figure 3.10: Relation of the gimbal rotation axes (red) to the optical axis and approximate focal point of the camera (blue). The gimbal  $x$  axis and the optical axis are parallel (but not collinear) when the gimbal is at zero azimuth and elevation.

be a significant problem, since typical ten-camera videogrammetry capture volume is not more than a few meters on each side, and the minimum focal distance of the PTZ cameras is 1.5 m. This location method is preferred for its ease of use, but it is not always possible to implement.

The gimbal objects are defined by placing retroreflective markers on the bottom fixed servo and creating an object in the videogrammetry software. The origin of the newly defined object must then be manually translated to the intersection of the gimbal axes. This is done with the aid of temporary markers placed on the camera approximately on the axes of the gimbal. Finally, the gimbal is rotated to zero azimuth angle, and the  $x$  axis of the object coordinate system is rotated to align with the camera's optical axis. When the gimbal is placed in the videogrammetry capture volume, the location and orientation is generated and can be passed to the aiming software.

Videogrammetry markers can be located to sub-millimeter accuracy, and so the accuracy of the location of the gimbal origin is limited only by the ability to place the temporary markers on the gimbal axes for correct alignment of the object coordinate system. The directions of the gimbal axes are well-defined on the gimbal, by the rotating shafts extending outside the case.



The three methods described above provide a variety of ways to locate the PTZ cameras. Camera location is a necessary step for aiming, zooming and focusing the cameras on a moving object.

### 3.4 *Lens*

Photogrammetric accuracy is primarily dependent upon the resolution of the object in images used for processing. Therefore it is desirable for the test object to fill as much of the frame as possible. Zoom and focus lenses are used to maintain a sharp image and a desired viewing radius at the distance of the object.

Four closed circuit television lenses are used to control aperture, magnification, and focus of the pan-tilt-zoom cameras. Commands are sent to the lens via 16 bit serial protocol. The lens is capable of viewing angles from  $29^\circ$  to  $2^\circ$ , and can focus on objects as close as 1.5 m. The lens can frame and focus on a 0.5 m diameter sphere at any distance between 1.75 m and 14 m, although typical distances in the current lab are between 1.75 m and 4 m.

The magnification and focus settings for each lens are determined from the distance of the object and the desired field of view at that distance. In the system, the lens acts as a varifocal lens, in that the magnification and the focus are functions of one another; however, the effect of changing the focus on the magnification was minimal across all magnification settings, and so was neglected.

Functions of magnification and focus were determined from collected data. First, the angle of view was recorded for seven magnification settings, with the focus setting at its minimum. An empirical equation was developed for the magnification setting as a function of the viewing angle using a least squares fit of a polynomial curve to interpolate between the points. Letting  $r$  be the distance to the object and  $d$  be the width of the field of view at that distance, the viewing angle  $\omega$  is given by

$$\omega = 2 \arctan(d/2r) \tag{3.8}$$

Note that a maximum  $\omega$  of  $19^\circ$  is found at the minimum distance of 1.5 m and largest typical viewing radius of .25 m in the lab. A fifth order polynomial of the form

$$Z_s = c_0 + c_1\omega + c_2\omega^2 + c_3\omega^3 + c_4\omega^4 + c_5\omega^5 \quad (3.9)$$

was found to produce good magnification results. Figure 3.11(a) shows the curve fit and the data points. At large  $\omega$  the curve fit is unrealistic, but for values of  $\omega$  below  $19^\circ$  the curve adjusts the field of view with sufficient accuracy.

The focus setting function was derived using a bivariate interpolation of magnification and focus data. Magnification and focus data were collected at six distances, and six hyperbolic polynomials were fit to these data. The choice of function and polynomial order were made based on observation of general trends in the data. Let  $F_s$  be the focus setting.

$$F_s = a_0 + a_1(1/Z_s) + a_2(1/Z_s)^2 \quad (3.10)$$

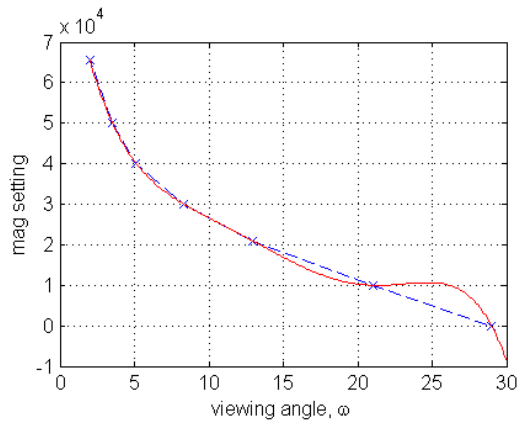
where  $a_0$ ,  $a_1$  and  $a_2$  are polynomial coefficients. Another set of 1st order polynomials were fit to the coefficients as a function of distance, shown in Figure 11(b).

$$a_i = b_{i,0} + b_{i,1}r \quad i = 0, 1, 2 \quad (3.11)$$

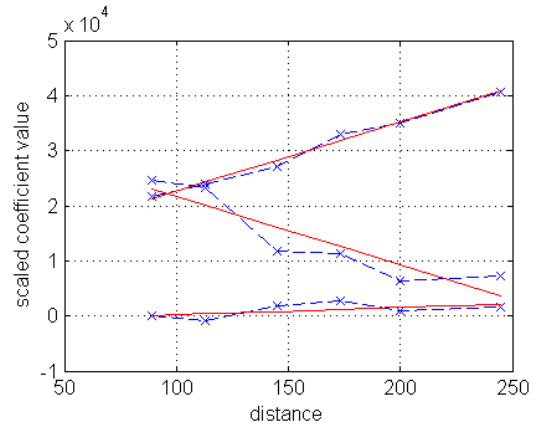
and so

$$F_s = \sum_{i=0}^2 (b_{i,0} + b_{i,1}d) \left( \frac{1}{Z_s} \right)^i \quad (3.12)$$

Figure 3.12 shows the initial data and the distances at which it was gathered in blue and the curve fits based on that data in red. Although the curve fits do not match the data very well in some regions, especially at the edges of the capture volume, in the typical region for this lab the curve fits are reasonable. The green hashed line shows the lower distance limit from the camera and two lines of constant field of view (FOV) at which typical test articles are photographed.



(a) Graph of lens magnification setting vs viewing angle.



(b) Graph of focus polynomial coefficients

Figure 3.11: Graph of data and curve fits for magnification and focus polynomial coefficients

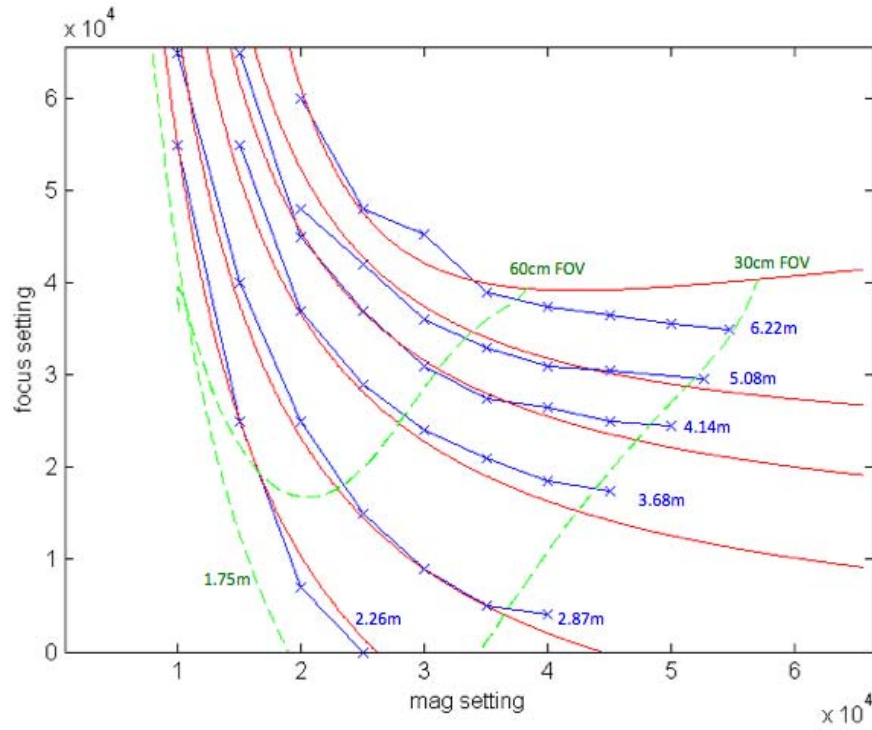


Figure 3.12: Graph showing the magnification and focus data (blue), the curve fit approximations (red) and the typical domain of the lens settings in the current lab (green).

Note also that at short distances the focus setting appears to be very sensitive to the magnification setting. The 2.26 m distance curve covers the entire range of focus settings over only approximately 15,000 units of magnification. This is somewhat misleading. While it is true that optimal focus is highly dependent on magnification on these curves, the depth of focus is increased at lower magnification settings. Therefore there is a greater tolerance for error in the focus setting, and conditions that according to this graph are less than ideal nonetheless produce suitable images.

Another feature to notice in Figure 3.12 is trimming of part of the domain at low FOV settings and short distances. This effect must be taken into account when preparing the camera system for image capture. The PTZ cameras may need to be placed further outside the capture volume for smaller objects.

Figure 3.13 illustrates the entire process of calculating the lens settings. This method of generating the focus and magnification settings provides good clarity and framing of an object within the capture volume. Combining the aiming, zoom and focus systems produces the PTZ camera system which provides framing and focusing from four viewpoints.

### 3.5 Camera

Each camera is capable of taking 500 frames per second at 1280x1024 pixel resolution. Synchronous image capture is achieved by having the cameras capture frames based on an external trigger. The trigger is generated by a hardware timer in the control computer and sent to each of the cameras.

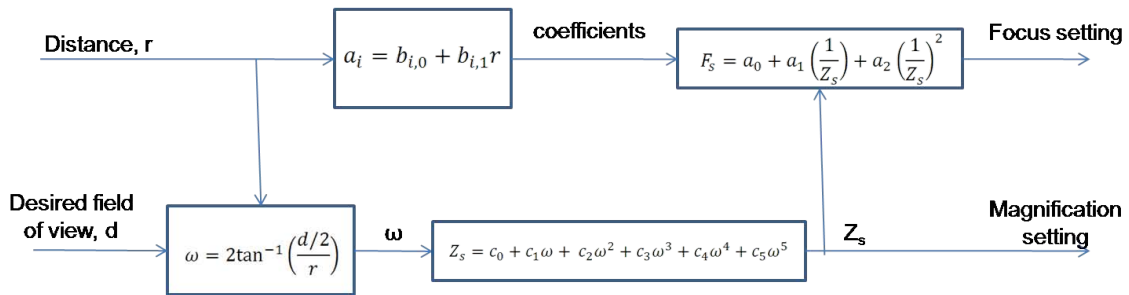


Figure 3.13: Schematic describing the calculation of magnification and focus settings

### 3.6 *Computers and Software*

Each of the four cameras that comprise the PTZ camera system has a dedicated computer containing control software and image storage. The control software is used for calculating and communicating gimbal and lens commands as described above and to record current gimbal and lens states. Another software package performs image capture and records the images to a 2 terabyte RAID<sup>3</sup> array. A fifth computer is used to generate the trigger signal for the cameras, and it can also be used to control each of the four camera computers over the network so that an image capture can be set up and run from one station. The 3-D position of a test object is obtained from the videogrammetry system software run on a dedicated computer. All computers are connected with a gigabit local area network. Figure 3.14 illustrates the communication between the software and hardware.

The PTZ controller software is implemented in the data-flow programming software LabVIEW<sup>4</sup>. The controller consists of four main parts: Data acquisition from the videogrammetry software, gimbal controller, lens controller, and lens and gimbal state recorder. These parts are placed in separate programming loops for optimal speed for each part. Figure 3.15 shows the control software interface.

Data acquisition is accomplished using a .NET library supplied by Vicon. The controller software uses this library to call for the location and orientation of specific objects from the videogrammetry software. If the camera is registered as a videogrammetry object, its location is requested at the beginning of tracking also. The videogrammetry system produces data at 120 Hz at full 16 megapixel resolution.

The gimbal controller implements the aiming algorithm described in Sections 3.3 and 3.4. At each iteration of the gimbal loop, the azimuth and elevation is calculated and compared to the previous command. If the change is greater than a certain threshold, the command is sent to the gimbal. Azimuth and elevation are sent at one time and additional commands to new angles override previous ones. If the change is less than the threshold, no command is sent to the gimbal in order to avoid unnecessary use when the

---

<sup>3</sup>Redundant Array of Independent Disks

<sup>4</sup>National Instruments Corporation, 11500 N Mopac Expwy. Austin, TX 78759-3504

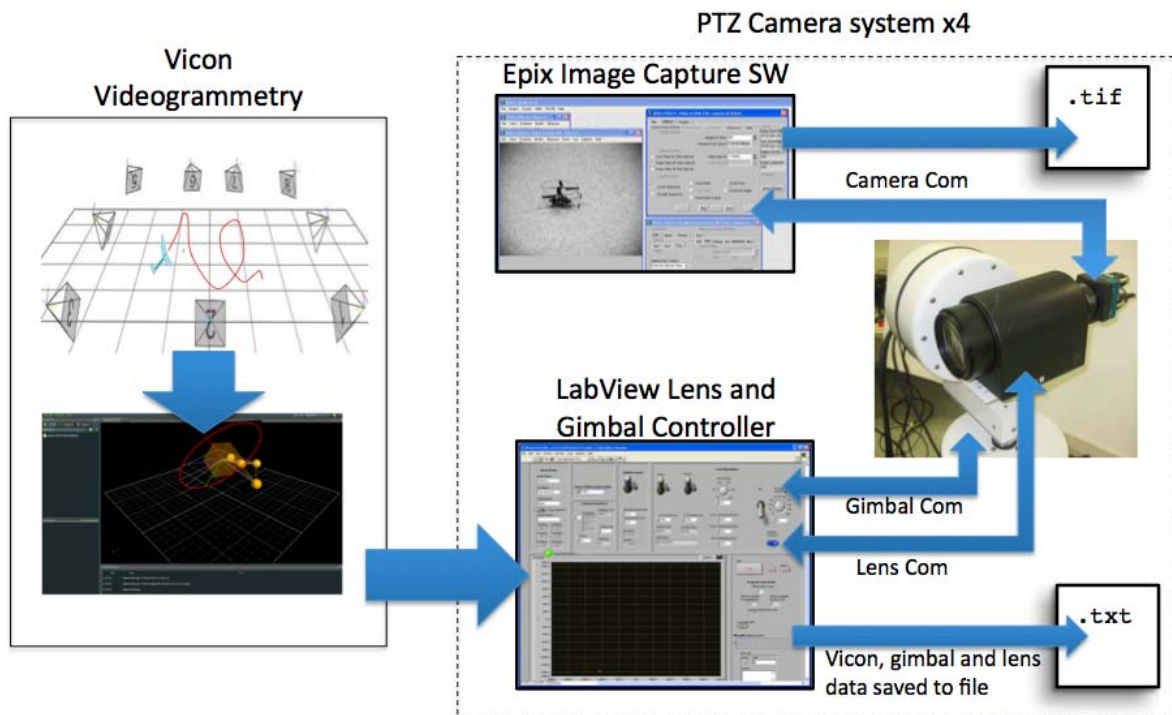


Figure 3.14: System software and hardware communication

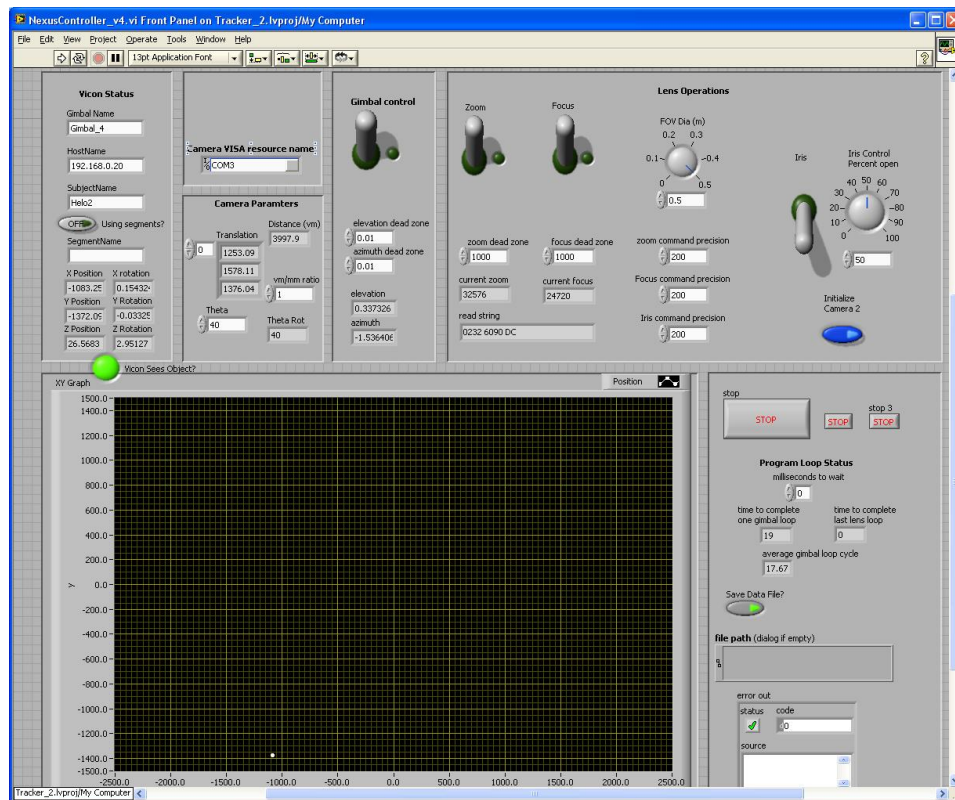


Figure 3.15: The lens, gimbal and lens and gimbal state recording is controlled with the interface shown.

tracked object is stationary. Typical thresholds are  $0.01^\circ$ . Whether or not a command is sent, the controller program queries the current azimuth and elevation of the gimbal.

The lens controller implements the focus and zoom algorithm described above. The appropriate zoom and focus setting is calculated, and a similar thresholding is applied as to the gimbal. Typical threshold values for both zoom and focus are 1,000 units. The commands must be sent in a series; sending a focus command before the zoom command is completed will interrupt the zoom. Waiting for previous commands to complete limits how quickly new commands can be sent. After each command, the lens state is queried repeatedly as the setting changes, resulting in knowledge of the zoom and focus settings throughout the change.

The gimbal and lens controller loops run at the maximum speed allowed by each device. The gimbal loop averages approximately 15 ms for one iteration when no movement command is sent, and 22 ms when commands are sent. The lens loop must wait until each zoom and focus command is completed before restarting and potentially sending a new command. The time this takes varies depending on how large a change is directed, but can be 500 ms or more.

The object location, gimbal state, and lens state are all saved into an array for use in photogrammetric image processing in a data recording loop. The recording loop is a timed loop that runs with a 5 ms period in order not to miss any data from the other loops. Additionally, the recording loop period and loop iteration is recorded to alert to any error in timing. The timing of this loop is critical, as it will be the basis of synchronizing the gimbal and lens state information with the image sequence.

The images and the lens and gimbal state data are used by the photogrammetry software to generate surface profiles. The state data, in particular the zoom setting of the lens, is used to determine the camera calibration parameters as is described in the next chapter. With the calibration parameters, the images can be processed and 3-D point locations found.

### ***3.7 Image Processing***

Image processing is performed with the commercial photogrammetry software PhotoModeler Scanner. The software contains subpixel marking tools, coded target recognition, and texture-based photogrammetry tools.

Although common image processing routines are well developed and automated within PhotoModeler, dynamic tracking and measurement requires additional flexibility due to the dynamic internal and external camera parameters, the motion of the test object, and the large number of images to be processed. The necessary custom automation can be brought about by controlling PhotoModeler externally using dynamic data exchange and a scripting software such as MATLAB. The majority of the photogrammetry processes, with the notable current exception of texture-based surface mapping, can be controlled in this way.

### ***3.8 Test Equipment***

The dynamic accuracy of the aiming system was measured using a rotation table shown previously in Figure 3.4. The rotation table allowed infinite duration movement along a circular path. The mounting platform at the end of the arm counterrotates with the turntable itself by means of a gear and belt system. This keeps the mounted object facing the same direction and all points on the object maintaining the same speed throughout the rotation. A box with several coded targets on its face was defined in the videogrammetry software and was tracked for the dynamic tests.



## IV. System Tests and Results

FOUR primary tests were performed to evaluate the capabilities of the DTM system, and their methodology and results are presented in this chapter. First, a description of the use of curve fits for determining calibration parameters is given and an analysis of suitability of this approach is presented. Image synchronization is demonstrated. The camera aiming error is evaluated the the limits it places on PTZ tracking is discussed. Finally, the tracking and image capture of a MAV in flight is presented and shown to correspond to the predicted camera aiming performance.

### 4.1 *Camera Calibration*

Determining the 3-D location of a point based on its two dimensional position on the photographic plane requires an accurate camera model. Typically, the parameters of the model are solved for with a camera calibration. For a fixed-parameter camera, the parameters can be solved for by taking 8-12 images of a calibration grid and performing a bundle adjustment using photogrammetry software such as PhotoModeler. However, as stated before, many of the camera calibration parameters are functions of the zoom, focus, and aperture of the lens, and so a new camera model is needed for every combination of these settings. This dependence poses a significant problem to the designer of a photogrammetry system which allows the zoom and focus settings to change freely throughout a sequence of images. The calibration parameters must be derived as a function of a known value, such as the zoom and focus settings.

### 4.2 *Development of Parameter Curves*

For the DTM system, empirical functions were developed for the camera model parameters based the calibration data from many lens conditions. This method for calibrating the pan-tilt-zoom cameras is a modified version of the approaches in References [10] and [12], which were described in section 2.1.3. In both papers, the camera parameters which were determined have the greatest effect on the photogrammetry results and to be the easiest to model were the principal point location  $(x_0, y_0)$ , first distortion parameter  $k_1$ , and focal length  $f$ .

The camera parameters chosen for this model were  $f$ ,  $k_1$ , and  $k_2$ . These parameters were chosen primarily for the ease with which they could be modeled. Their values as a function of zoom setting showed clear trends which enabled reliable curve fitting. Numerous calibrations showed the values of decentering distortion parameters  $p_1$  and  $p_2$  had little effect on the bundle adjustment solution and usually were automatically removed by the calibration algorithm. Principal point parameters were held constant for simplicity but will be considered for inclusion in future work.

The camera model is based on the model presented in section 2.1.2 and is given in Equation 4.1

$$M \begin{bmatrix} X - X_L \\ Y - Y_L \\ Z - Z_L \end{bmatrix} = \frac{1}{k} \begin{bmatrix} x - x_0 + dx \\ y - y_0 + dy \\ -f \end{bmatrix} \quad (4.1)$$

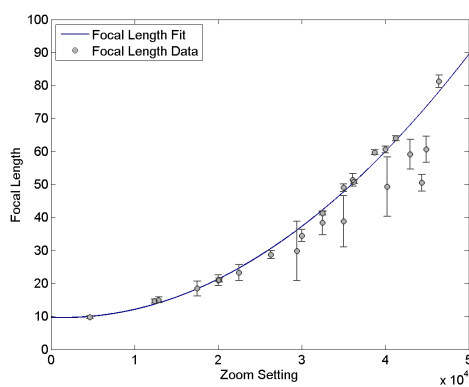
where

$$dx = k_1(x - x_0)r^2 + k_2(x - x_0)r^4 \quad (4.2)$$

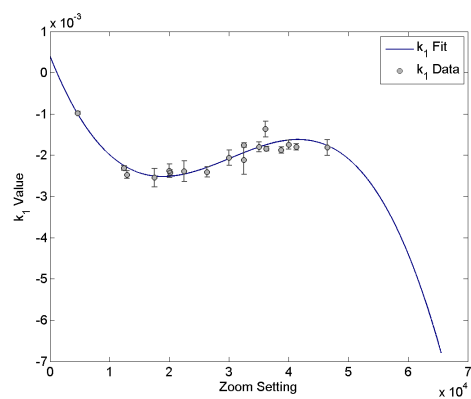
$$dy = k_1(y - y_0)r^2 + k_2(y - y_0)r^4 \quad (4.3)$$

The parameters  $f$ ,  $k_1$ , and  $k_2$  were calculated using PhotoModeler's self-calibration algorithm. Twenty-two zoom and focus points in the normal operating range of the lens were calibrated. The aperture was fixed at full dilation and was not considered for dependence. The data showed that the parameters were a much stronger function of the zoom setting than the focus, as was expected, and so the parameters were developed as a functions of zoom only. Curves were fit to the data based on a weighted least squares approximation, where the weight for each data point is the inverse square of the RMS residual value produced by the PhotoModeler calibration. These curve fits are shown in Figure 4.1.

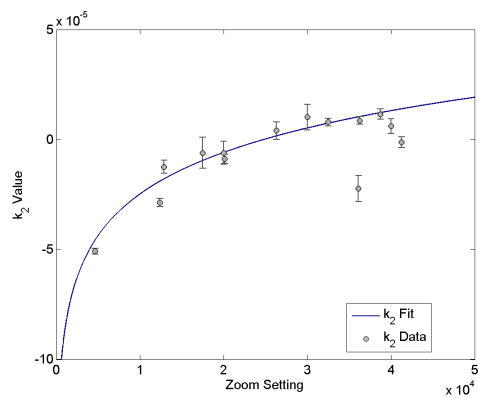
These curves allow for efficient estimation of the calibration parameters from the zoom setting, which is recorded during image capture, avoiding a lengthy self-calibration at each time step.



(a) Focal length curve fit



(b)  $k_1$  parameter curve fit



(c)  $k_2$  parameter curve fit

Figure 4.1: Graphs showing calibration parameter data and curve fits. Error bars are based on calibration quality and determine weights given to data points

### 4.3 Test of Curve-fit Parameters

The performance of the photogrammetric processing with the use of curve-fit parameters was evaluated by comparing the resulting point locations with those when using parameters generated by a partial and full calibration. This test is intended to give some insight into the error incurred by using a less sophisticated camera model, and then interpolating the camera parameters between calibration points.

The following metrics were used for the evaluation. The internal consistency of a point cloud is determined by the RMS residual and tightness value. The residual gives the two-dimensional distance of the location of the point in a particular image from the location of the solution point generated from all the images. The tightness value is similar, but is the 3-D distance from the particular image point to the solution point. Absolute point accuracy was measured against the “truth” point cloud generated from fully calibrated parameters. The RMS point error was calculated in each direction as well as the total RMS error. Since photogrammetric accuracy is dependent on the resolution of the object in the image, the error is also written as a ratio of the approximate height of the image, 500 mm. Therefore, for this test, pixel resolution is 1:1000, and millimeter resolution is 1:500.

Comparisons were made at three zoom and focus settings within the DTM envelope shown in Figure 3.12. At each setting, a set of images were taken of the calibration grid like the one shown in Figure 4.2 and described in Table 4.1. All pictures were taken with one PTZ camera. The calibration grid was rotated between images and the PTZ camera was held fixed.

The vantage points for the images for lens condition one is shown in Figure 4.3. Condition two and three had similar configurations at increasing distance, except at

Table 4.1: Data on the calibration grid used in the curve-fit tests

no. of points	144
no. of coded points	4
length of side	536 mm
approx. scale factor	0.5 mm/pixel

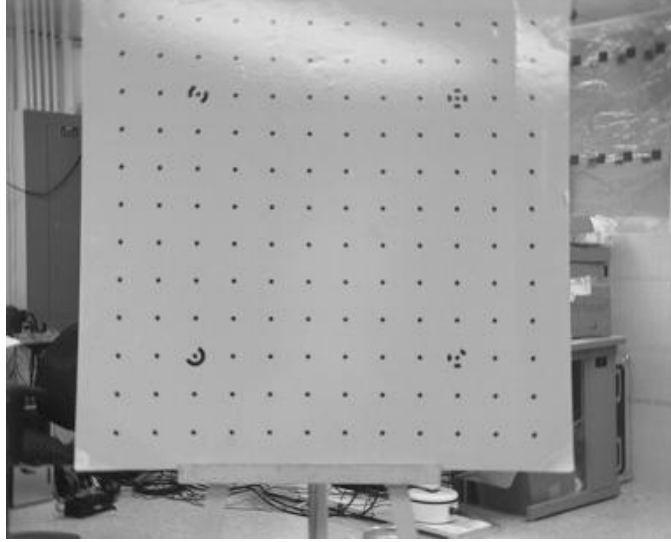


Figure 4.2: PhotoModeler calibration grid. 8-12 images of the grid from different angles are processed to generate calibration parameters at a specific lens setting.

condition three the four images with the highest angle of incidence were removed because they interfered with the stability of the calibration. Twelve images were used at the short and medium focal length, and eight were used at the long focal length.

Three point clouds were generated at each lens condition using the same image set. All points were subpixel marked in each image for maximum accuracy. The first point cloud was generated by performing a full calibration, which calculates camera parameters and point locations for the grid. The full calibration allowed PhotoModeler to decide which camera parameters to include to give the best result. The camera parameters included were  $f$ ,  $k_1$ ,  $k_2$ ,  $x_0$ , and  $y_0$ . The second point cloud was generated with a partial calibration which held fixed the principal point and solved for  $f$ ,  $k_1$ , and  $k_2$ . The third point cloud was generated using curve-fit calibration parameters and the same principal point as the partial calibration. The value at which the principal point was fixed was the average of three values from prior calibrations at the zoom settings. The three sets of points will be referred to as the full calibration (FC) point cloud, the partial calibration (PC) point cloud, and curve-fit parameter (CP) point cloud.

Tables 4.2, 4.3, and 4.4 show the results at the three zoom settings. The first thing to notice is that the PC point cloud had similar and sometimes better residual and tightness than the FC point cloud. This is an encouraging result, since it indicates that

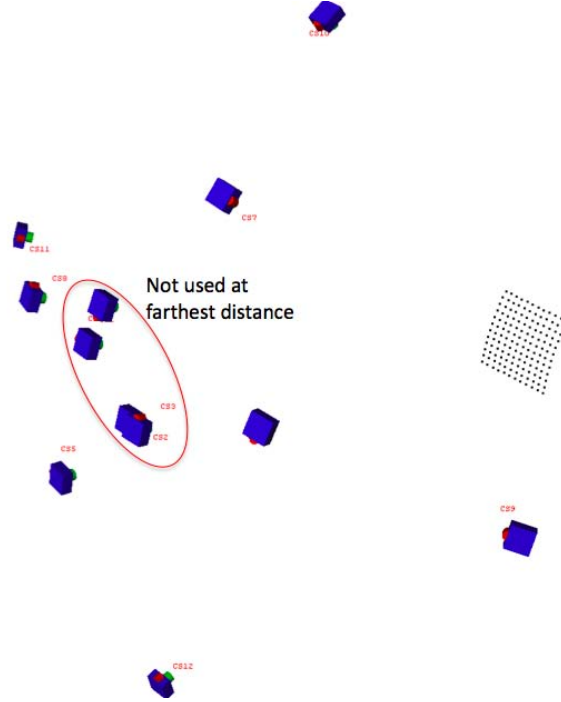


Figure 4.3: Approximate camera locations for lens condition one and two. Lens condition three did not have the four locations with highest angle of incidence.

the upper limit of the internal consistency of the reduced camera model is as good as that of the full camera model. Internal consistency is therefore solely a function of the quality of the curves that are fit to the parameter values.

Accuracy of the PC point clouds decrease with increasing focal length, but since the full and partial calibrations are of similar internal consistency, it is questionable whether the full calibration produced significantly more accurate point locations to be considered “truth”. Only large differences in the comparison of tightness value between point clouds can be considered an indication of relative accuracy. An independent measurement of the point locations should be considered for a more reliable comparison of accuracy.

The CP point cloud showed a significant decrease in tightness compared to the PC and FC point clouds. Accuracy was on the order of a pixel. This is a relatively low value for point accuracy in comparison with general photogrammetry, (see Reference [10]), although it would still be acceptable in certain cases. The low accuracy and tightness is most likely caused by a poor focal length curve-fit. This is indicated by the fact that

the tightness of the CP point cloud improved at higher zoom setting and lower percent difference between the curve-fit and calibrated focal lengths.

As further evidence of the need to improve the focal length curve, consider the residual directions for the images used for processing lens condition one. Figure 4.4 shows the residuals for the PC point cloud, which do not exhibit a strong pattern that would indicate poor modeling. Compare that to Figure 4.5. The images with lower incidence angles (image 9, 10, 11, and 12, the bottom row) clearly show that point calculations for those images were less trapazoidal than the overall point locations. This is caused by the camera having been calculated to be farther from the grid of points than it actually was, which in turn caused it to expect less of a perspective angle than was actually the case. The distance of the camera is calculated from the focal length, and a larger focal length is equivalent to larger distance.

The poor focal length curve fit is a correctable problem. Additional calibrations can be taken with special attention to the consistency of the parameters at each zoom setting. Instead of weighting the calibration results, fewer calibrations should be performed with a emphasis on low residuals and tightness. The performance of the partial calibration indicates that high accuracy and tightness are possible with this camera model, and an improvement of the focal length curve-fit will be a step in the right direction. Though the current curve-fits are not optimal, the results of this test indicate that this is a suitable approach for calibrating the PTZ camera system in a dynamic environment.

The previous test showed the accuracy of the calibration curve fits under a controlled situation with twelve images. The test shows the upper limits of accuracy with the current system. An actual image capture, however, will be taken with multiple cameras, and will have only four images to process. The image viewpoints, which have a significant impact on point accuracy and precision, will not be able to be controlled.

To demonstrate a photogrammetry project under these circumstances, the following example was performed. A flat board was covered with coded photogrammetry targets and four point clouds were generated using calibrated cameras and good viewing angles. These point locations were averaged and considered truth. The truth surface was compared to four additional point clouds. The comparison clouds were generated

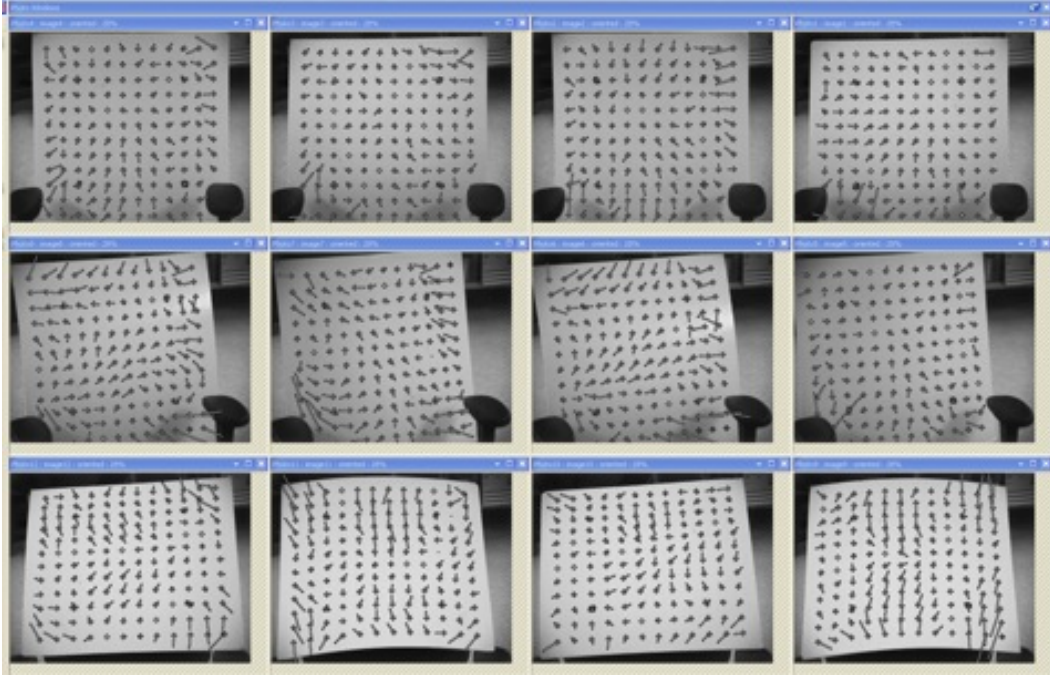


Figure 4.4: Residual direction and relative scale of each point in each image for PC point cloud in test one

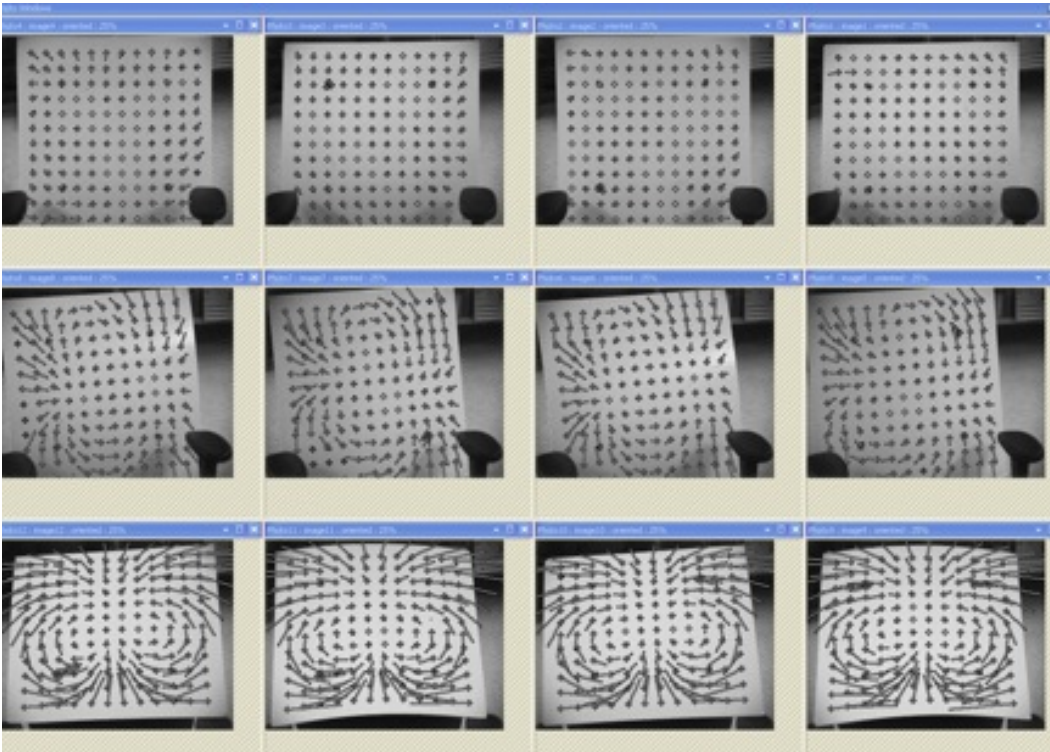


Figure 4.5: Residual direction and relative scale of each point in each image for CF point cloud in test one



Table 4.2: Comparison of point cloud data at lens condition 1

Lens Condition 1				
Zoom Setting – 25700, Focus Setting – 21673				
		Full Calibration	Partial Calibration	Curve-fit Parameters
Camera Parameters	$f$ (mm)	27.8874	27.9101	32.65
	$k_1$	-2.059e-3	-2.097e-3	-2.228e-3
	$k_2$	-2.487e-5	-3.855e-6	2.852e-6
	$x_0$	2.9733	2.9772	2.9772
	$y_0$	2.4870	2.4802	2.4802
RMS residual (pixels)		.0867	.0878	.87
Tightness	mm	.131	.128	1.38
	ratio	1:4000	1:4,000	1:400
RMS error	mm		.0306	.595
	ratio		1:18,000	1:900
RMS error Directional	$x$		.00927	.0927
	$y$		.0117	.145
	$z$		.0267	.569

Table 4.3: Comparison of point cloud data at lens condition 2

Lens Condition 2				
Zoom Setting – 31993, Focus Setting – 27349				
		Full Calibration	Partial Calibration	Curve-fit Parameters
Camera Parameters	$f$ (mm)	37.8998	37.9645	41.2521
	$k_1$	-2.112e-3	-2.102e-3	-1.966e-3
	$k_2$	1.870e-5	1.623e-5	6.991e-6
	$x_0$	2.981	2.9772	2.9772
	$y_0$	2.4821	2.4802	2.4802
RMS residual (pixels)		.1213	.1034	.41
Tightness	mm	.186	.1456	.618
	ratio	1:3000	1:4,000	1:900
RMS error	mm		.0700	.284
	ratio		1:8,000	1:2,000
RMS error Directional	$x$		.0108	.0737
	$y$		.0123	.0794
	$z$		.0680	.190

Table 4.4: Comparison of point cloud data at lens condition 3

		Lens Condition 3		
		Zoom Setting – 38702, Focus Setting – 33026		
		Full Calibration	Partial Calibration	Curve-fit Parameters
Camera Parameters	$f$ (mm)	52.4612	52.6104	56.6318
	$k_1$	-2.053e-3	-1.997e-3	-1.664e-3
	$k_2$	1.431e-5	1.442e-5	1.22e-5
	$x_0$	2.9758	2.9772	2.9772
	$y_0$	2.4778	2.4802	2.4802
RMS residual (pixels)		.1213	.1089	.30
Tightness	mm	.189	.1319	.3542
	ratio	1:3000	1:4,000	1:1,500
RMS error	mm		.1542	.7294
	ratio		1:4,000	1:700
RMS error Directional	$x$		.0682	.495
	$y$		.1277	.449
	$z$		.0530	.1949

using all four PTZ cameras on the outside of the room and the photogrammetry object placed in the center. Four images of the object were taken for each point cloud, and the object was rotated  $90^\circ$  between each set. Each set was processed using curve fit calibration parameters and the error for each point is shown in Figure 4.6. In order to observe internal error alone, the point clouds were corrected for errors due to translation, rotation and scaling by minimizing the error with respect to those parameters, and the corrected error values also are also shown in Figure 4.6. These corrections were small, with translations, rotations, and scale factors less than 0.5 mm,  $1^\circ$ , and 1% respectively. Note that the error in positions 1 and 3 are approximately double that of 2 and 4, and since the object was rotated  $90^\circ$  between positions, positions 1 and 3 were in similar but reverse orientations. In these positions, the object was in a less favorable orientation, with the majority of the markers at a shallower angle than in positions 1 and 4. The transformed error normalized by the object length is approximately 1:400 for positions 2 and 4, and 1:200 for positions 1 and 3. Thus it can be see that image orientation of

the images can have a negative effect on the point cloud accuracy. More information on the effects of object orientation and can be found in reference [6].

The results of the curve fit calibration parameters test indicate the viability of using even very basic curve-fitting for generating calibration parameters. Point clouds generated under operational conditions show additional loss of accuracy, but it is supposed that this will improve with improved curve fits. Refinement of the curve fit calibrations will be the subject of future work. The use of this method allows the generation of calibration parameters on a continuous scale, and is key to enabling the use of the pan-tilt-zoom cameras for dynamic photogrammetry.

#### ***4.4 Validation of Image Synchronization***

For dynamic reconstruction of objects in motion to be accurate, it is important that each set of four images be synchronized. The synchronization system described above was validated with the following test. A sequence of images was captured of a small direct current electric motor running at approximately 11 revolutions per second. Attached to the motor is a paper “fan” with a drawing on one side, so that its orientation can be determined. The trigger signal was run at 500hz and the cameras were set up to capture images on the rising edge of the signal. The four images in Figure 4.7 are image 352 of each of the sequences, and although the fan image is not sharp due to the exposure time, the darker area caused by the drawing on the left side shows that it has the same orientation in each of the images. This assures that the system has the capability of synchronous image capture to within one frame. However, by analyzing the blur of the fan tip and noting its beginning and end in each photo, it appears to be even better than that.

#### ***4.5 Validation of Tracking System***

The tracking system has two parts: the camera aiming, accomplished by the gimbal, and the focus and zoom, controlled by the lens. Each are controlled with separate loops in the PTZ controller software as described in section 3.6, and they both pose limits on the ability of the PTZ cameras to produce suitable images for photogrammetry. The

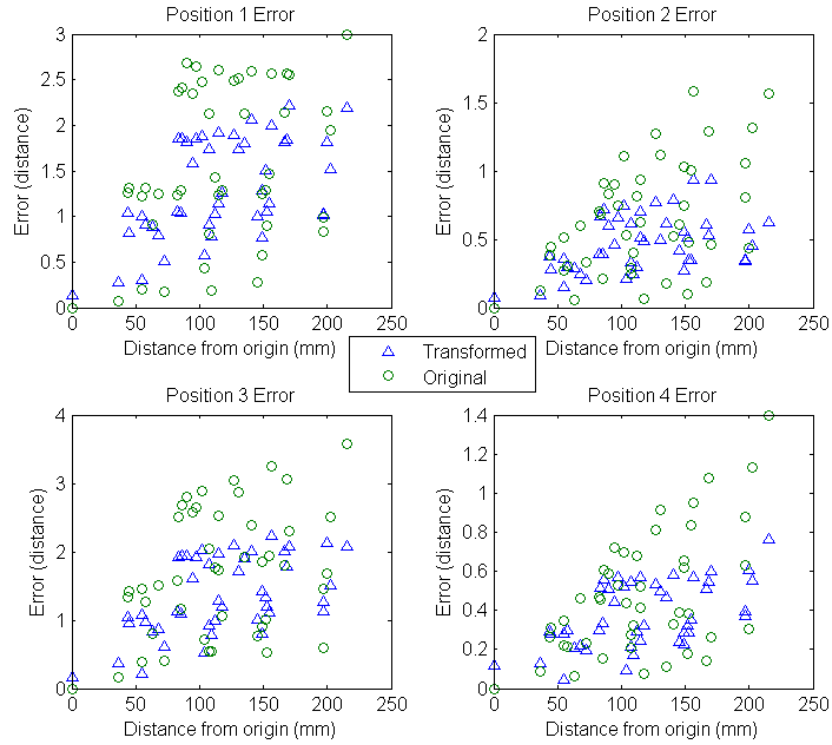


Figure 4.6: Error for four photogrammetry projects compared to the truth surface. Circles denote raw points and triangles denote points scaled, translated and rotated for optimum fit. Points are plotted against scalar distance from origin. The object is rotated  $90^\circ$  between each position.

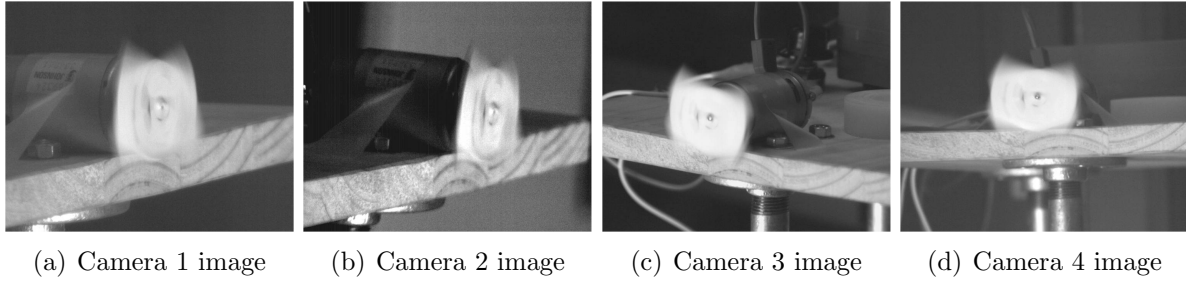


Figure 4.7: The four high-speed cameras capturing synchronous images at 500fps. Note that the spinning paper “fan” has the same orientation with respect to the mounting platform in each image.

following section describes the tests run to evaluate the capabilities of the gimbal and its effects on camera aiming. The lens analysis was not performed for this thesis.

Total camera aiming error is the result of several factors. Static pointing error results from approximations made in the aiming algorithm and camera location and orientation error. Dynamic error is mostly caused by the gimbal dynamics, with additional dynamic error caused by time lag from the videogrammetry system, control software, and serial communication. As a first step in determining and reducing the error caused by each of these factors, the total aiming error was evaluated.

Initial validation of the aiming system was performed by tasking the camera to track a videogrammetry object attached to the rotation table in Figure 3.4. The object maintained its orientation as it spun, and four coded photogrammetry targets were placed on the side facing the camera. The coded targets are round markings that are automatically marked and referenced between frames by the photogrammetry software. One target was placed at the aiming point, and the others were placed near the  $x$  and  $y$  axis limits of the object for scaling purposes.

The regular motion of the rotation table allowed the position and orientation of the tracked object to be known in each frame without synchronizing the image capture with the videogrammetry system. This allowed any delay in the processing of the videogrammetry data to be included in the error assessment. The radius and center of the circular path was determined by the least squared error of the center to the position minus the

radius squared

$$e_{cf} = \sum_{i=1}^n ((x_i - \hat{x})^2 + (y_i - \hat{y})^2 - \hat{r}^2)^2 \quad (4.4)$$

where  $e_{cf}$  is the circle fit error,  $x_i$  and  $y_i$  are positions generated by the videogrammetry system, and  $\hat{x}$ ,  $\hat{y}$ , and  $\hat{r}$  are the center location and radius. The radius  $\hat{r}$  can be written in terms of the other variables

$$\hat{r} = \sqrt{\frac{1}{n} \sum_{i=1}^n ((x_i - \hat{x})^2 + (y_i - \hat{y})^2)} \quad \hat{r} \neq 0 \quad (4.5)$$

and using the notation  $\bar{x}$  to designate the mean,  $\hat{x}$  and  $\hat{y}$  can be solved for from two simultaneous equations

$$2 \begin{bmatrix} \sum_{i=1}^n (x_i(x_i - \bar{x})) & \sum_{i=1}^n (x_i(y_i - \bar{y})) \\ \sum_{i=1}^n (x_i(y_i - \bar{y})) & \sum_{i=1}^n (y_i(y_i - \bar{y})) \end{bmatrix} \begin{bmatrix} \hat{x} \\ \hat{y} \end{bmatrix} = \begin{bmatrix} \sum_{i=1}^n (x_i^2(x_i - \bar{x}) + y_i^2(x_i - \bar{x})) \\ \sum_{i=1}^n (x_i^2(y_i - \bar{y}) + y_i^2(y_i - \bar{y})) \end{bmatrix}. \quad (4.6)$$

The turntable was rotated at a constant speed using motors and a belt drive, and an LED<sup>1</sup> was triggered to flash when the object passed a certain point in the rotation. The LED flash could be seen in the PTZ camera as it tracked, which allowed the period and phase of the rotation to be determined directly from the images. The period, phase, and radius of the rotation table was used to generate the function for the continuous periodic truth input to which the tracking error and output was compared.

Fifteen tracking tests were run; six rotating the table in each direction at a distance of 2.5 m and speeds ranging from 0.2 m/s to 0.9 m/s, and three at approximately 0.55 m/s and increasing distance to a maximum of 4.25 m. During each test the PTZ camera captured a sequence of images at 30 frames per second and in each image the distance between the target point and the image center was measured in pixels, as shown in Figure 4.8. The additional scaling targets were used to determine a pixel to mm scale factor

---

<sup>1</sup>light-emitting diode

in each direction for each image. The millimeter error summed with the truth function produced the output of the camera system.

The motion of the object was separated into its  $x$  and  $y$  components, with  $x$  component of motion tracked by the azimuth servo of the gimbal and  $y$  component by the elevation servo. The millimeter error in each direction was measured and Figure 4.9 shows the results plotted versus object speed in meters per second. RMS values in the  $y$  direction are lower than the  $x$  because the angle of view causes the velocity perpendicular to the camera vector to be reduced. Test points marked by diamonds were run at distances greater than the 2.5 m, with the farthest distance being 4.25 m.

The fact that the diamond-marked points lie on the same curve as the other points indicate a minimal dependence of the millimeter tracking error on distance. This is because of the counterbalancing of the effects of angle error and angular velocity of the tracked object about the gimbal. At close range, the gimbal is required to rotate faster in order to track an object at a given speed than at a farther distance, thus causing a larger angular error. However, a large angular error at close range results in a smaller linear error at the object than when further away. Thus, the two effects cancel each other. Additional testing may show that the cancellation is not perfect, especially at extremely close and far distances, but in the lab capture volume it holds well.

The RMS angular error of the gimbal was found using the center of the rotation table as the average distance to the object. The RMS angular velocity of the gimbal required by the speed of the rotation table was calculated as shown in Equations 4.7 and 4.8

$$\omega_{az} = \sqrt{2}vd \quad (4.7)$$

$$\omega_{el} = \sqrt{2}\sin(\phi)vd \quad (4.8)$$

where  $v$  is the speed of the rotation table,  $d$  is the distance from the gimbal to the center of the rotation table, and  $\phi$  is the camera angle of incidence. The angular error was plotted against the angular velocity and is shown in Figure 4.10

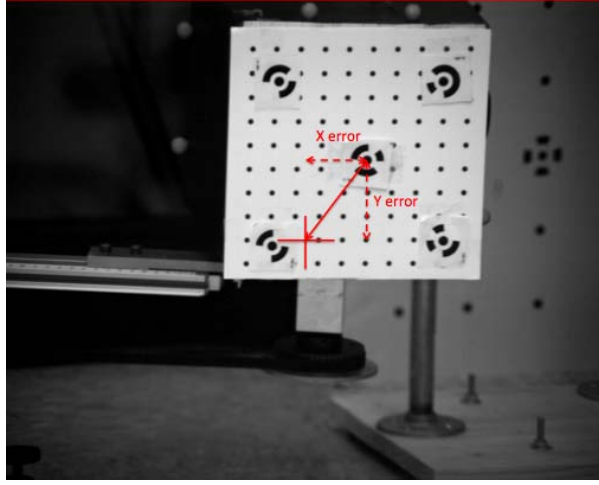


Figure 4.8: Camera aiming error is measured in pixels from the center image pixel to the coded target on the box.

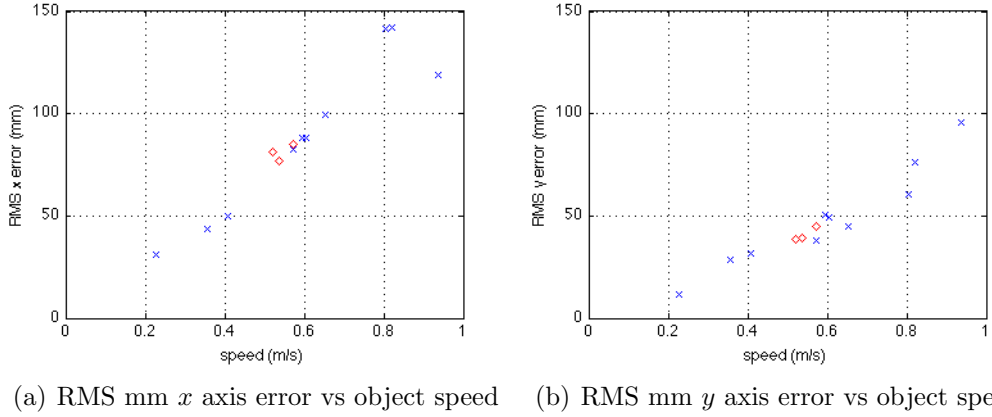
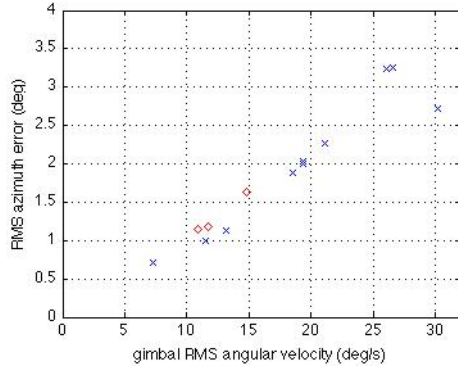


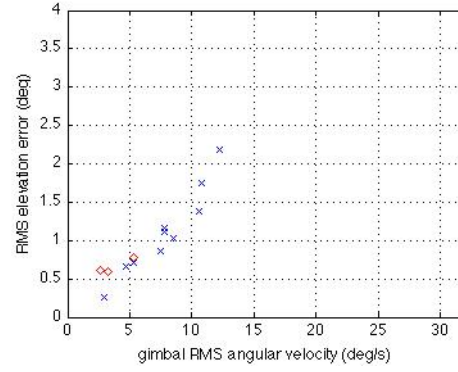
Figure 4.9: RMS mm error vs speed of rotation table. Points marked with x's were tested at 2.5 m from camera. Diamond points indicate tests run at increased distances.

Two notes should be made about the data. There is clearly more angular error in the elevation axis than the azimuth axis shown in Figure 4.10(b). This is most likely caused by the camera not being perfectly balanced on the gimbal, so that the gimbal has to overcome the effects gravity in addition to inertia when rotating to point downwards. The additional moment required by the gimbal in that direction slows the overall response time. Secondly, the drop in error for the final data point in Figures 4.9(a) and 4.10(a) are due to data dropout rather than a true reduction in error. At the peak amplitude and the highest turntable speed, the scaling targets were outside the field of view of the camera, and so no millimeter error could be calculated. When the RMS error was

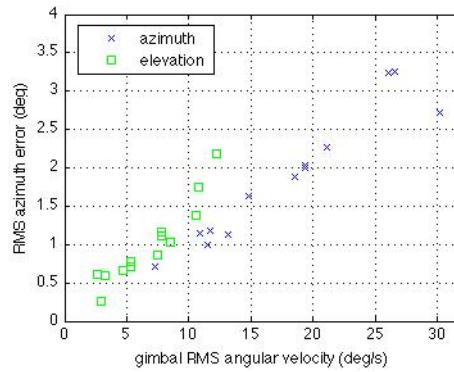




(a) RMS angular azimuth error vs angular velocity



(b) RMS angular elevation error vs angular velocity



(c) Combined azimuth and elevation error

Figure 4.10: RMS Angular error vs. RMS angular velocity of gimbal. Points marked with x's were tested at 2.5 m from camera. Diamond points indicate tests run at increased distances.

calculated for that point, the lack of the highest error data artificially reduced the RMS value. Nonetheless, this point was included for completeness, as it is included in the following phase shift analysis (where the data dropout does *not* effect the result).

The phase shift and magnitude change were calculated by fitting the output data to sinusoidal curves using a least squares method and then comparing its magnitude and phase to the truth input. Figure 4.11 show the resulting Bode plots.

The Bode plots will provide a valuable data source for modeling of the system dynamics. Future efforts to improve the aiming performance, such as adding a Kalman filter, will require a model of the system.

Increasing speed has the effect of reducing the resolution of the cameras by limiting how small a field of view can be used. For the ideal case, with perfect zoom and focusing such that the object remains the same size in all images, the number of pixels per unit length would be fixed, and the value would depend on the anticipated speed of the object. The object resolution,  $n_o$  pixels/object radius, is related to the maximum speed and radius of the object in the ideal case by

$$n_o = \frac{n_p/2}{r_{obj} + e_{mm}(v)} r_{obj} \quad (4.9)$$

where  $n_p$  is the number of pixels across the shortest dimension of the image plane,  $r_{obj}$  is the half the largest dimension of the object, and  $e_{mm}(v)$  is the RMS millimeter tracking error at speed  $v$ . Using current laboratory cameras with 1280x1024 resolution, and a typical object radius of 15 cm, the plot in Figure 4.12(a) was constructed. The plot indicates an expected decrease in resolution of the object speed increases. A second plot in Figure 4.12(b) shows the object resolution plotted vs. length of the object, and shows that larger objects can be covered with more pixels than smaller ones, even though the pixel/unit length value may decrease.

The camera aiming system described above is capable of keeping vehicles in the frame under the given restrictions of speed and resolution. To take a typical example, an object of 15 cm radius with a desired pixel resolution of 1.7 pixel/mm would be limited to speeds less than 0.9 m/s. The system generally favors large, slow moving vehicles, because it is able to cover these vehicles with more pixels per object size. There are several ways in which this system could be improved. One is the addition of a Kalman filter, which uses predicted future position of the object to improve aiming accuracy. Another possibility is to use a custom gimbal controller that puts a greater premium on error reduction, at the expense of such effects as overshoot. The gimbal is capable of using a custom controller, which is important for continuing development of the tracking system.

#### 4.6 Tracking Example: Helicopter

To demonstrate the tracking system, a sequence of images was captured of a MAV in flight. The MAV is a radio-controlled helicopter with two counterrotating rotors and two smaller maneuvering rotors shown in Figure 4.13. The helicopter was marked with 6 mm retroreflective videogrammetry targets and defined as an object in the videogrammetry software. All four PTZ cameras were set to track and image the helicopter as it was flown. The field of view was set in the PTZ controller at 0.5 m. Nine hundred synchronous images were taken at 30 fps with a shutter speed of 5 ms, for a total capture time of 30 seconds.

The location of the helicopter was recorded during image capture. The location data at several time steps is missing, however, because at those time steps the videogrammetry system had lost the helicopter. This occurs at only a small number of locations, and the gaps are clearly visible in the location and speed plots. This problem was caused by using a calibration of the videogrammetry system that was several days old. A new calibration would reduce and possibly eliminate data dropout.

The  $x$  and  $y$  location of the helicopter is shown in Figure 4.14, and the  $z$  location is plotted with respect to image number in Figure 4.15(a). A rough plot of the instantaneous speed of the the helicopter is given in Figure 4.15(b). The speed was calculated by taking the backwards-difference of the position measurements and dividing by the time interval, shown in Equation 4.10.

$$v_i = \frac{|[x_i, y_i, z_i] - [x_{i-1}, y_{i-1}, z_{i-1}]|}{t_i - t_{i-1}} \quad (4.10)$$

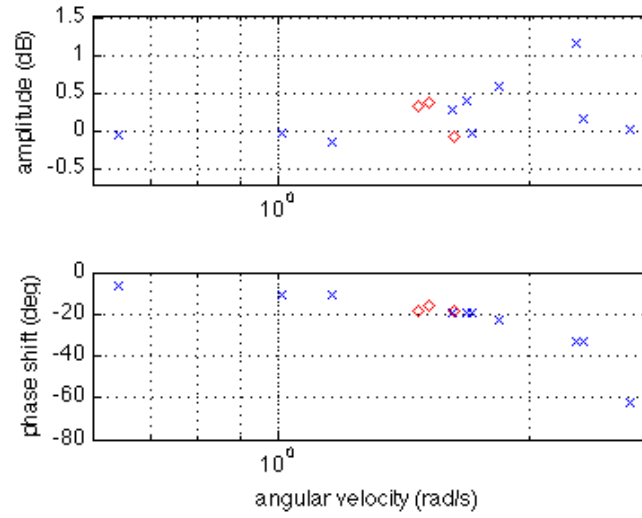
The time interval was varied until a value was found that appeared to be a good balance between resolution and noise reduction.

The helicopter began on the ground, and was flown smoothly to altitude. At approximately image 510 the helicopter lost altitude rapidly and hit the ground, then recovered after a low sweeping turn. This area is circled in Figure 4.14 and the drop and speed increase is clearly visible in Figures 4.15(a) and 4.15(b). The helicopter recovered altitude slowly and the capture ends in mid-flight.

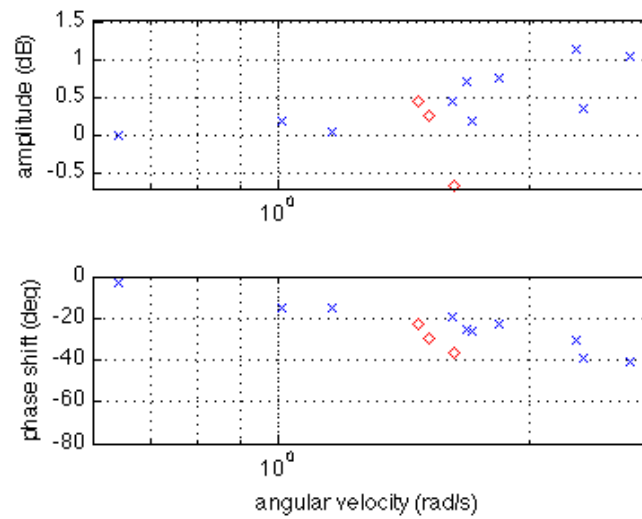
Figures 4.16 and 4.17 show an excerpt of 30 images from the 900 image sequence from camera four. The images are at one-second intervals and the image number is listed below each. During the initial ascent, with speed peaking at about 0.8 m/s, the helicopter remains in view of the camera. At image 540, the helicopter is completely outside the camera frame, and does not fully recover until image around 600. The loss of the vehicle occurs during the high-speed descent, when a speed of approximately 1.8 m/s is reached.

The helicopter remains in focus until the end of the sequence, around frame 780 to 810. As this occurs while the helicopter is moving relatively slowly away from the camera, the lens is likely the limiting factor in the speed at which objects can be tracked. A thorough analysis of the lens is needed to determine what that limit is.

This example shows the ability of the tracking system to maintain focus and framing of a flying vehicle. The performance of the system during the capture is shown to generally match the predicted performance in the previous section. This system will provide an effective means of gathering images suitable for photogrammetry in a dynamic environment, a unique capability.

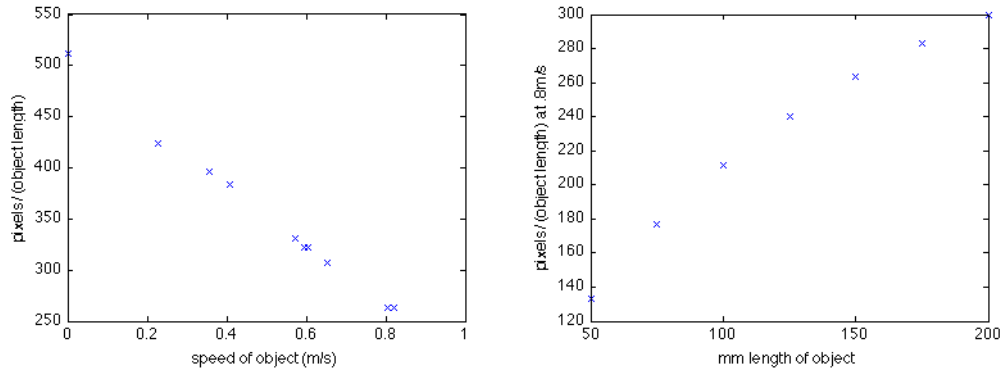


(a)  $x$  axis magnitude and phase



(b)  $y$  axis magnitude and phase

Figure 4.11: Bode plots of tracking data. Points marked with x's were tested at 2.5 m from camera. Diamond points indicate tests run at increased distances.



(a) Pixels per radius of object vs. object speed at 15cm object radius. (b) Pixels per radius of object vs. radius of object at 0.8 m/s speed.

Figure 4.12: Resolution as a function of object speed and size, assuming ideal lens operation.

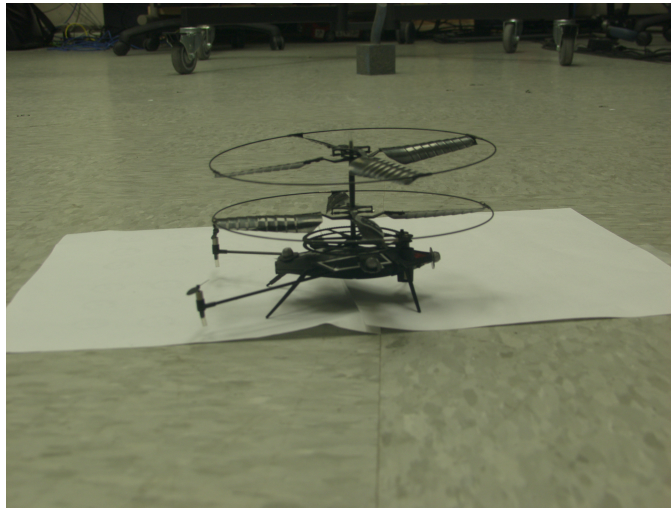


Figure 4.13: Twin rotor helicopter used in example capture

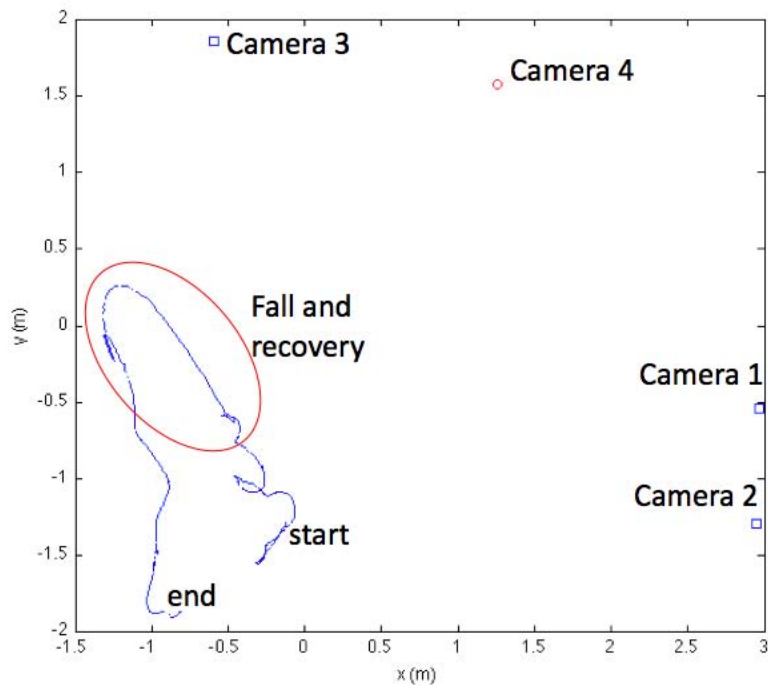
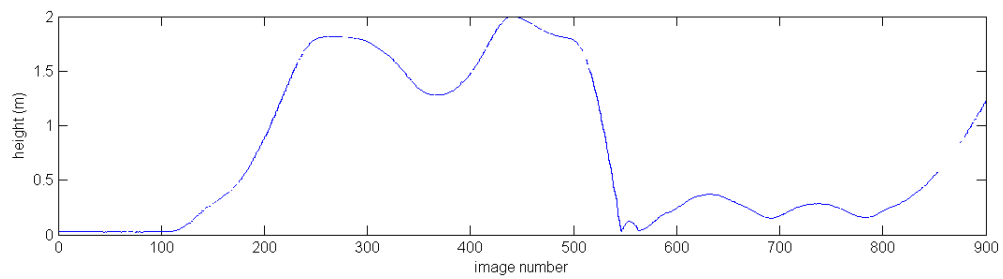
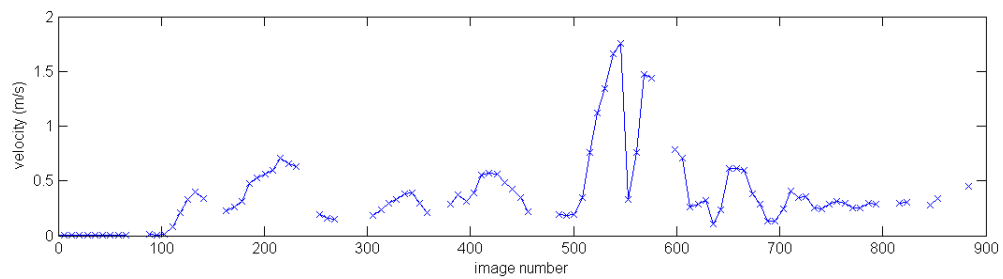


Figure 4.14: Helicopter and camera  $x$ - $y$  locations during image capture



(a) Helicopter speed vs. image number



(b) Helicopter speed vs. image number

Figure 4.15: Helicopter speed and height during image capture



Figure 4.16: Images of helicopter from camera 4 at one second intervals



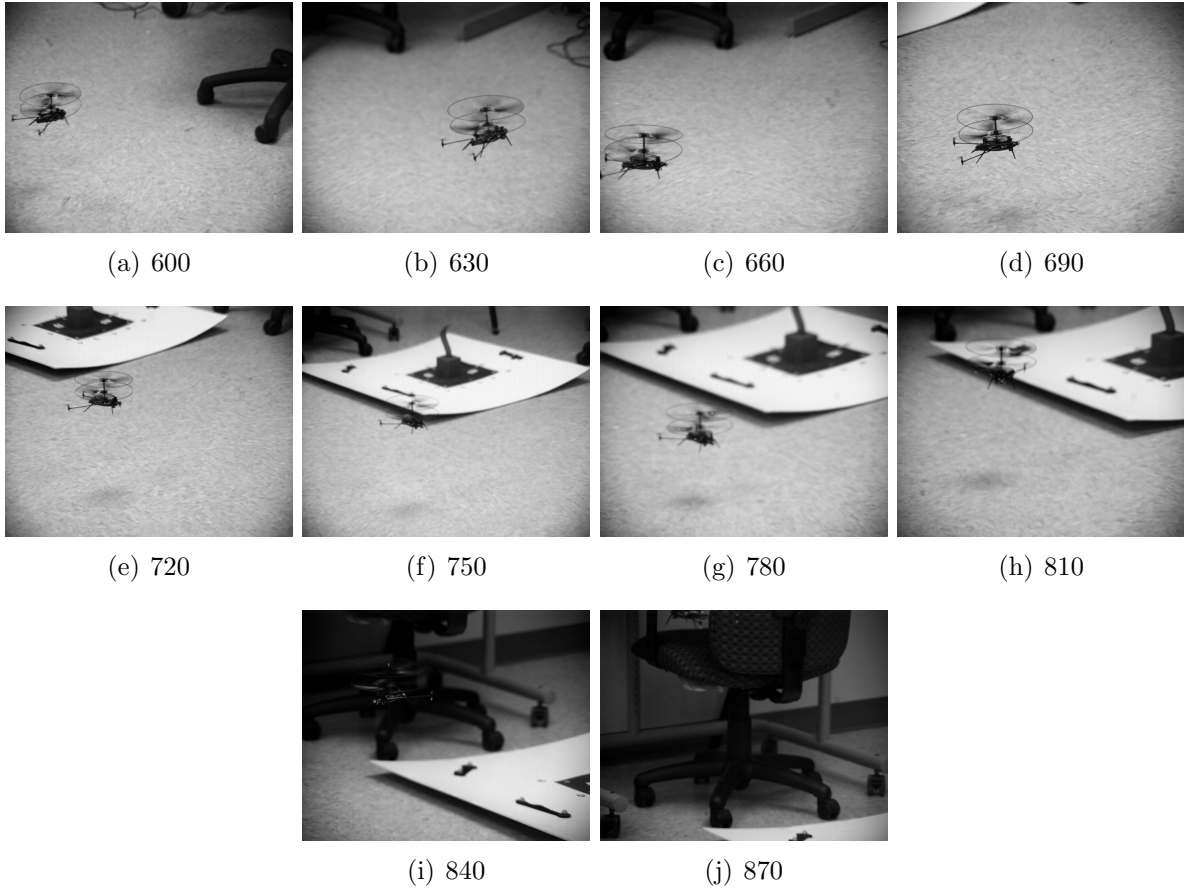


Figure 4.17: Images of helicopter from camera 4 at one second intervals

## V. Conclusions and Future Work

### 5.1 Conclusion

THIS thesis developed and evaluated a hybrid DTM system for collecting kinematic measurements of structural surfaces in motion. The system will provide unique data sets on objects such as MAVs in flight and deployable space structures that will aid in the design and development of these systems.

The system components were described, and details were given on the control and integration of the cameras. Calculation of the azimuth and elevation angles for the gimbals was presented. Multiple methods of locating the cameras were presented and compared, and location by the videogrammetry system was shown to be the preferred method because of its ease of use and robustness. The method of calculating the zoom and focus settings to maintain a constant field of view was developed and the envelope of the zoom and focus was outlined. The tracking system was combined and controlled in a computer program and details of its operation were addressed.

Several test of the system were performed to evaluate performance and find areas needing improvement. The tests were: analysis of the use of curve fits for calibration parameters, demonstration of camera synchronization, analysis of dynamic camera aiming error, and a demonstration of the system tracking and taking images a MAV in flight.

Using curve fit parameters for dynamic photogrammetry is a novel technique. The technique was tested to determine if it would produce accurate and precise point clouds. Point clouds generated with curve fit calibration parameters were compared to those generated with partial and full calibrations. The resulting curve fit point clouds were found to have an accuracy around 1 unit error per thousand (1:1,1000), which is equivalent to pixel-sized error, and RMS residual around 0.5 pixels. The focal length parameter generated by curve fit was significantly higher than those generated by partial and full calibrations, and analysis of the residual directions indicates that the focal length curve fit is the primary source of point error and low precision. The reduced camera model that was used was shown to have comparable precision to the fully calibrated cameras. This result indicated that with improvement of the curve fits, especially the focal length curve fit, accuracy of around 1:10,000 can be expected.

Camera synchronization was established by taking a capture with all four cameras at 500 fps of a rotating motor. The motor was shown to be in the identical orientation in each camera, indicating that all four images were taken synchronously.

The dynamic camera aiming error was evaluated and found to be within reasonable limits. The dependence of maintaining view of an object on the object speed and the field of view was described, and the relationship between object speed and allowable object resolution was presented. It was shown that speeds approaching 0.9 m/s are attainable with 1.7 pixel/mm resolution and 15 cm object. As an example of the tracking system in operation, a sequence of images of a MAV flying in the lab was shown. The system was able to frame and focus on the vehicle throughout most of the 30 s flight, and the performance of the system approximately followed the predicted performance.

Based on the results shown here, this photogrammetry-based hybrid DTM system is capable of tracking and recording the necessary image data for generating surface profiles of lightweight dynamic structures. The hybrid measurement concept that this system is based on overcomes the limitations of the individual systems and allows a new look at the behavior of lightweight structures. It has the potential to be expanded by adding additional sensors along with the PTZ cameras, such as laser vibrometers and laser range finders. In conclusion, the measurement system presented in this thesis has the capability to give researchers new insight into lightweight structures in a natural environment, and the possibilities offered by the hybrid measurement approach are only just beginning to be explored.

## **5.2 Future Work**

Future work on the DTM system will focus on finishing the characterization of the system with an analysis on the lens and the limitations it places on object tracking. Lens analysis will include determining how quickly the lens can adjust zoom and focus, and how focus error affects the photogrammetric processing. Additional improvement of the system with a custom designed closed loop gimbal controller has the potential to reduce aiming error. Improvement of the curve fit parameters will likely increase photogrammetric accuracy.

Since the purpose of the system is the photogrammetric reconstruction of objects in motion, methods of automating the processing of image data are needed. Generating surface profiles is currently a labor-intensive process, and manual processing of potentially thousands of frames of image data is not practical. Initial steps have been taken in automating the processing such as controlling the photogrammetry software with a computer script, and future work will build on this start.

## Bibliography

1. Dorrington, A. A., Jones, T. W., Danehy, P. M., and Pappa, R. S., "Laser-Induced-Fluorescence Photogrammetry for Dynamic Characterization of Membrane Structures," *AIAA Journal*, Vol. 42, No. 10, 2004, pp. 2124–2129.
2. Markley, J., Stutzman, J., and Harris, E., "Hybridization of Photogrammetry and Laser Scanning Technology for As-Built 3D CAD Models," *IEEE Aerospace Conference*, March 2008, pp. 1–10.
3. Wolf, P. R. and Dewitt, B. A., *Elements of Photogrammetry*, McGraw-Hill, New York, NY, 3rd ed., 2000.
4. Mikhail, E. M., Bethel, J. S., and McGlone, J. C., *Modern Photogrammetry*, John Wiley & Sons, Inc., New York, NY, 1st ed., 2001.
5. Gruen, A., "Fundamentals of videogrammetry - A review," *Human Movement Science*, Vol. 16, 1997, pp. 155–187.
6. Jennings, A. L., Allen, C., Magree, D., Black, J. T., Jameson, M., Rogers, D., and Pollock, S. A., "Effect of Camera Setup on Photogrammetry Texture-Based Surface Reconstruction," *Submitted to Structures, Structural Dynamics, and Materials Conference*, AIAA, May 2010.
7. Giersch, L. R. M., "Pathfinder Photogrammetry Research for Ultra-Lightweight and Inflatable Space Structures," *NASA Langley Research Center*, Vol. NASA/CR-2001-211244, 2001.
8. Clarke, T. A., Fryer, J. G., and Wang, X., "The principal point and CCD cameras," *Photogrammetric Record*, Vol. 16, No. 92, 1998, pp. 293–312.
9. Eos Systems, Inc., *PhotoModeler User Guide*, 210 - 1847 West Broadway, Vancouver, BC V6J 1Y6.
10. Fraser, C. and Sl-Ajlouni, A., "Zoom-dependent camera calibration in digital close-range photogrammetry," *Photogrammetric Engineering & Remote Sensing*, Vol. 72, No. 9, 2006, pp. 1017–1026.
11. Remondino, F. and Fraser, C., "Digital camera calibration methods: considerations and comparisons," .
12. Willson, R. G., *Modeling and Calibration of Automated Zoom Lenses*, Phd dissertation, Department of Electrical and Computer Engineering, Carnegie Mellon University, 1994, online at [http://www-old.ri.cmu.edu/pubs/pub\\_1443.html](http://www-old.ri.cmu.edu/pubs/pub_1443.html).
13. Blandino, J. R., Pappa, R. S., and Black, J. T., "Modal Identification of Membrane Structures with Videogrammetry and Laser Vibrometry," *Structures, Structural Dynamics and Materials Conference*, Vol. AIAA-2003-1745, Norfolk, Virginia, April 2003, pp. 1–11.
14. Pappa, R. S., Black, J. T., Blandino, J. R., Jones, T. W., Danehy, P. M., and Dorrington, A. A., "Dot Projection Photogrammetry and Videogrammetry of Gossamer Space Structures," *AIAA Journal of Spacecraft and Rockets*, Vol. 40, No. 6, 2003, pp. 858–867.

15. Leifer, J., Black, J. T., Smith, S. W., Ma, N., and Lump, J. K., "Measurement of In-Plane Motion of Thin-Film Structures Using Videogrammetry," *Journal of Spacecraft and Rockets*, Vol. 44, No. 6, Nov-Dec 2007, pp. 1317–1325.
16. Black, J. T., Pitcher, N. A., Reeder, M. F., and Maple, R. C., "Videogrammetry Measurements of a Lightweight Flexible Wing in a Wind Tunnel," *Journal of Aircraft*, Vol. 47, No. 1, 2010, doi: 10.2514/1.44545, also AIAA Paper 2009-2416.
17. Lin, S.-Y., Mills, J. P., and Gosling, P. D., "Videogrammetric monitoring of as-built membrane roof structures," *The Photogrammetric Record*, Vol. 23, No. 122, 2008, pp. 128–147.
18. Valenti, M., Bethke, B., Fiore, G., How, J. P., and Feron, E., "Indoor Multi-Vehicle Flight Testbed for Fault Detection, Isolation, and Recovery," *Guidance, Navigation and Control Conference*, Vol. AIAA-2006-6200, Keystone, Colorado, Aug 2006, pp. 1–18.
19. Bellmann, A., Hellwich, O., Rodehorst, V., and Yilmaz, U., "A Benchmarking Dataset for Performance Evaluation of Automatic Surface Reconstruction Algorithms," *Computer Vision and Pattern Recognition, 2007. CVPR '07. IEEE Conference on*, June 2007, pp. 1–8.
20. Curtis, D. H., Reeder, M. F., Svanberg, C. E., and Cobb, R. G., "Flappin Wing Micro Air Vehicle Bench Test Set-up," *Aerospace Sciences Meeting*, Vol. AIAA 2009-1272, Orlando, FL, January 2009.
21. Aono, H., Wu, S. K. C. R., Sällström, E., Stanford, B. K., Cesnik, C. E. S., Ifju, P., Ukeiley, L., and Shyy, W., "A Computational and Experimental Study of Flexible Flapping Wing Aerodynamics," *Aerospace Sciences Meeting*, Vol. AIAA 2010-554, Orlando, FL, January 2010.
22. Chakravarty, U. K. and Albertani, R., "Experimental and Finite Element Modal Analysis of a Pliant Membrane for Micro Air Vehicles Wings," *AIAA Structures, Structural Dynamics, and Mechanics Conference*, Vol. AIAA 2010-2710, Orlando, FL, April 2010.
23. Pappa, R. S., Geirsch, L. R., and Quagliaroli, J. M., "Photogrammetry of a 5-m Inflatable Space Antenna with Consumer-Grade Digital Cameras," *Experimental Techniques*, 2001, pp. 21–29.
24. How, J. P., Bethke, B., Frank, A., Dale, D., and Vian, J., "Real-Time Indoor Autonomous Vehicle Test Environment," *IEEE Control Systems Magazine*, April 2008, pp. 51–64.
25. Saad, E., Vian, J., Clark, G. J., and Bieniawski, S., "Indoor Multi-Vehicle Flight Testbed for Fault Detection, Isolation, and Recovery," *InfotechAerospace Conference*, Vol. AIAA-2009-1824, Seattle, Washington, April 2009, pp. 1–9.
26. Halaas, D. J., Bieniawski, S. R., Pigg, P., and Vian, J., "Control and Management of an Indoor, Health Enabled, Heterogenous Fleet," *InfotechAerospace Conference*, Vol. AIAA-2009-2036, Seattle, Washington, April 2009, pp. 1–19.

27. Troy, J. J., Erignac, C. A., and Murray, P., "Closed-Loop Motion Capture Feedback Control of Small-Scale Aerial Vehicles," *InfotechAerospace Conference*, Vol. AIAA-2007-2905, Rohnert Park, California, April 2007, pp. 1–14.
28. Hahne, D. E. and Fremaux, C. M., "Low-Speed Flight Dynamic Tests and Analysis of the Orion Crew Module Drogue Parachute System," *Atmospheric Flight Mechanics Conference*, Vol. AIAA-2008-6391, Honolulu, Hawaii, Aug 2008, pp. 1–13.
29. Velasquez, L. E. and Rajulu, S. L., "Evaluation of a Non-Video Based Mobility Tracking System for Suited Operations," *Space Conference*, Vol. AIAA-2004-6136, San Diego, California, Sept 2004, pp. 1–24.
30. Scoville, Z. C. and Rajula, S., "SAFER Inspection of Space Shuttle Thermal Protection System," *Space Conference*, Vol. AIAA-2005-6722, Long Beach, California, Sept 2005, pp. 1–18.
31. Ol, M., Parker, G., Abate, G., and Evers, J., "Flight Controls and Performance Challenges for MAVs in Complex Environments," *Guidance, Navigation and Control Conference*, Vol. AIAA-2008-6508, Honolulu, Hawaii, Aug 2008, pp. 1–21.
32. Ma, C.-C. and Hsieh, D.-M., "Full-Field Experimental Investigations on Resonant Vibration of Cracked Rectangular Cantilever Plates," *AIAA Journal*, Vol. 39 of 12, 2001, pp. 2419–2422.
33. Dharamsi, U. K., Evanchik, D. M., and Blandino, J. R., "Comparing Photogrammetry with a Conventional Displacement Measurement Technique on a 0.5m Square Kapton Membrane," *Structures, Structural Dynamics and Materials Conference*, Vol. AIAA-2002-1258, Denver, Colorado, April 2002, pp. 1–10.
34. Lin, S.-Y. and Mills, J. P., "Integration of videogrammetry and terrestrial laser scanning for dynamic surface modelling," *Videometrics VIII*, Vol. 5665, 2005, pp. 243–251.
35. Lamond, B. and Watson, G., "Hybrid Rendering – A New Integration of Photogrammetry and Laser Scanning for Image Based Rendering," *Proceedings of the Theory and Practice of Computer Graphics*, Vol. 0-7695-2137-1, 2004.
36. Zhou, X., Collins, R. T., Kanade, T., and Metes, P., "A Master-Slave System to Acquire Biometric Imagery of Humans at Distance," *International Workshop on Visual Surveillance*, Vol. ACM 1-58113-780-X/03/00011, 2003.
37. Bimbo, A. D., Dini, F., Lisanti, G., and Pernici, F., "Exploiting distinctive visual landmark maps in pan-tilt-zoom camera networks," *Computer Vision and Image Understanding*, Vol. 2010.01.007, 2010.
38. Simpkins, J., Sollars, R., Jennings, A. L., Allen, C., and Black, J. T., "Calibration and Performance of Laser Steering System for Measuring Moving Objects," *Smart Structures\ Nondestructive Evaluation and Health Monitoring, Proced. of SPIE*, Vol. 7292, SPIE, March 2009, pp. 7292–131.
39. Simpkins, J., Sollars, R., Jennings, A. L., Allen, C., and Black, J. T., "Calibration and Performance of Laser Steering System for Measuring Moving Objects," *Structures, Structural Dynamics, and Materials Conference*, AIAA, May 2009.

<b>REPORT DOCUMENTATION PAGE</b>			Form Approved OMB No. 0704-0188		
<p>The public reporting burden for this collection of information is estimated to average 1 hour per response, including the time for reviewing instructions, searching existing data sources, gathering and maintaining the data needed, and completing and reviewing the collection of information. Send comments regarding this burden estimate or any other aspect of this collection of information, including suggestions for reducing this burden to Department of Defense, Washington Headquarters Services, Directorate for Information Operations and Reports (0704-0188), 1215 Jefferson Davis Highway, Suite 1204, Arlington, VA 22202-4302. Respondents should be aware that notwithstanding any other provision of law, no person shall be subject to any penalty for failing to comply with a collection of information if it does not display a currently valid OMB control number. PLEASE DO NOT RETURN YOUR FORM TO THE ABOVE ADDRESS.</p>					
1. REPORT DATE (DD-MM-YYYY) 06/17/2010		2. REPORT TYPE Master's Thesis		3. DATES COVERED (From — To) August 2008 – June 2010	
4. TITLE AND SUBTITLE A Photogrammetry-Based Hybrid System for Dynamic Tracking and Measurement			5a. CONTRACT NUMBER		
			5b. GRANT NUMBER		
			5c. PROGRAM ELEMENT NUMBER		
6. AUTHOR(S) Daniel P. Magree			5d. PROJECT NUMBER 09ENY309		
			5e. TASK NUMBER		
			5f. WORK UNIT NUMBER		
7. PERFORMING ORGANIZATION NAME(S) AND ADDRESS(ES) Air Force Institute of Technology Graduate School of Engineering and Management (AFIT/ENY) 2950 Hobson Way WPAFB OH 45433-7765			8. PERFORMING ORGANIZATION REPORT NUMBER AFIT/GAE/ENY/10-J01		
9. SPONSORING / MONITORING AGENCY NAME(S) AND ADDRESS(ES) Air Force Office of Scientific Research AFOSR David Stargel 875 N Randolph St Ste 235 Rm 3112 Arlington, VA 22203			10. SPONSOR/MONITOR'S ACRONYM(S) AFOSR		
			11. SPONSOR/MONITOR'S REPORT NUMBER(S)		
12. DISTRIBUTION / AVAILABILITY STATEMENT APPROVED FOR PUBLIC RELEASE; DISTRIBUTION UNLIMITED					
13. SUPPLEMENTARY NOTES					
14. ABSTRACT Noncontact measurements of lightweight flexible aerospace structures present several challenges. Objects are usually mounted on a test stand because current noncontact measurement techniques require that the net motion of the object be zero. However, it is often desirable to take measurements of the object under operational conditions, and in the case of miniature aerial vehicles (MAVs) and deploying space structures, the test article will undergo significant translational motion. This thesis describes a hybrid noncontact measurement system which will enable measurement of structural kinematics of an object freely moving about a volume. By using a real-time videogrammetry system, a set of pan-tilt-zoom (PTZ) cameras is coordinated to track large-scale net motion and produce high speed, high quality images for photogrammetric surface reconstruction. The design of the system is presented in detail. A method of generating the calibration parameters for the PTZ cameras is presented and evaluated and is shown to produce good results. The results of camera synchronization tests and tracking accuracy evaluation are presented as well. Finally, a demonstration of the hybrid system is presented in which all four PTZ cameras track an MAV in flight.					
15. SUBJECT TERMS Photogrammetry, Test and Measurement, MAV, Space Structures, Hybrid Systems					
16. SECURITY CLASSIFICATION OF:			17. LIMITATION OF ABSTRACT  UU	18. NUMBER OF PAGES  84	19a. NAME OF RESPONSIBLE PERSON Dr. Jonathan T. Black, AFIT/ENY
a. REPORT  U	b. ABSTRACT  U	c. THIS PAGE  U			19b. TELEPHONE NUMBER (Include Area Code) (937)255-3636, ext